HHS Public Access

Author manuscript

Nat Struct Mol Biol. Author manuscript; available in PMC 2019 July 21.

Published in final edited form as:

Nat Struct Mol Biol. 2019 February ; 26(2): 96–109. doi:10.1038/s41594-018-0176-8.

Xist RNA antagonizes the SWI/SNF chromatin remodeler BRG1 on the inactive X chromosome

Teddy Jégu[*,1,2], **Roy Blum**[*,1,2], **Jesse C. Cochrane**[2], **Lin Yang**[1,2], **Chen-Yu Wang**[1,2], **Maud-Emmanuelle Gilles**[3], **David Colognori**[1,2], **Attila Szanto**[1,2], **Sharon K. Marr**[2], **Robert E. Kingston**[2], and **Jeannie T. Lee**[1,2]

[1]Howard Hughes Medical Institute

[2]Department of Molecular Biology, Massachusetts General Hospital, Boston, MA, USA; Department of Genetics, Harvard Medical School, Boston, MA, USA

[3]Institute for RNA Medicine, Department of Pathology, Cancer Center, Beth Israel Deaconess Medical Center, Harvard Medical School

Abstract

The noncoding RNA Xist recruits silencing factors to the inactive X chromosome (Xi) and facilitates re-organization of Xi structure. Here, we examine the mouse epigenomic landscape of Xi and assess how Xist alters chromatin accessibility. Interestingly, *Xist* deletion triggers a gain of accessibility of selective chromatin regions that is regulated by BRG1, an ATPase subunit of the SWI/SNF chromatin remodeling complex. In vitro, RNA binding inhibits nucleosome remodeling and ATPase activities of BRG1, while in cell culture Xist directly interacts with BRG1 and expels BRG1 from the Xi. Xist ablation leads to a selective return of BRG1 in cis, starting from pre-existing BRG1 sites that are free of Xist. BRG1 re-association correlates with cohesin binding and restoration of topologically associated domains (TADs), and results in formation of de novo Xi "superloops." Thus, Xist binding inhibits BRG1's nucleosome remodeling activity and results in expulsion of the SWI/SNF complex from the Xi.

Correspondence: lee@molbio.mgh.harvard.edu.

*These authors contributed equally to this work.

AUTHOR CONTRIBUTIONS

T.J., R.B. and J.T.L. designed the experiments and analyzed data. J.C.C. performed *in vitro* ATPase and remodeling assays. L.Y. performed the RNA-seq assays. D.C., A.S., and S.K.M. made all the plasmids. T.J. generated all data. R.B. performed all bioinformatics analyses, excepted the Hi-C analysis performed by C.Y.W. T.J. and M.E.G analyzed the immunoFISH. R.E.K. supervised J.C.C and S.K.M. T.J., R.B., and J.T.L. wrote the manuscript.

COMPETING INTERESTS STATEMENT

J.T.L. is a co-founder and serves on the scientific advisory boards of Translate Bio and Fulcrum Therapeutics.

Data availability.

ATAC-seq, nChIP-seq, and RNA seq data have been deposited in GEO under accession code GSE109395. All other data are available from the corresponding author upon reasonable request.

INTRODUCTION

In eukaryotic nuclei, each chromosome occupies a spatially defined “chromosome territory” (CT) during interphase. Microscopic studies reveal that CTs form a sponge-like structure that can be partitioned into “Inactive Nuclear Compartments” (INC) and “Active Nuclear Compartments” (ANC)[1,2]. Whereas transcriptionally silent and compacted heterochromatin form the INC compartment, accessible chromatin and actively transcribed regions form the ANC[1]. Molecular conformation studies have also shown that chromosomes are organized locally into “topologically associating domains” (TADs), domains of ~1 megabase within which chromatin tends to self-interact[3,4]. The borders that separate TADs are enriched for binding of architectural proteins such as cohesins and CTCF[3,5,6], whose orientation-dependent binding forms the basis of large-scale topological loops. 3D chromosome organization is currently thought to play important roles during development by modulating interactions between regulatory elements and their associated genes to produce diverse cellular phenotypes.

The mammalian X chromosome exemplifies this structure-function relationship during development. Mammalian female cells epigenetically silence one of their X chromosomes in order to equalize the levels of X-linked gene expression between the sexes. This process, called X-chromosome inactivation (XCI), generates an active X chromosome (Xa) and inactive X chromosome (Xi), and is regulated by the long noncoding RNA Xist[7–10]. Xist is strictly expressed from the Xi and spreads in cis to induce chromosome-wide silencing[11,12]. Silencing is accompanied by a dramatic re-organization of the 3D architecture. While the Xa is partitioned into TADs, the Xi is devoid of TADs and is instead segmented into two large domains, dubbed “megadomains”[5,13–15]. Xist plays an important role in maintaining this Xi-specific conformation by repelling cohesins and attenuating TAD structures[13]. Cytologically, XCI leads to a re-organization of the Xi CT, with a collapse of ANC at sites of Xist enrichment and gene repression[1]. Consistent with these findings, Xist induction correlates with decreased chromatin accessibility[14].

Although dramatic topological changes during XCI have come to light in recent years, the specific molecular factors underlying the complex changes have not been fully elucidated. Indeed, while Xist is known to recruit repressive complexes[16–19] and repel cohesins[13], Xist has yet to be connected to catalytic factors that directly drive changes in chromatin accessibility. A proteomic study identified a large number of epigenetic factors interacting with Xist, including ATP-dependent chromatin-remodeling complexes[13]. Nevertheless, functional characterization of these factors has yet to be undertaken. Here, we examine Xi chromatin accessibility and assess the effect of ablating Xist on the established landscape. Intriguingly, we reveal a differential sensitivity of Xi regions to Xist ablation, uncover a link to 3D Xi organization, and establish a functional antagonism between the BRG1 chromatin remodeling complexes and Xist, which underlies the heterogeneous organization of the Xi.

RESULTS

Differential dependence of Xi regions to Xist RNA

To investigate how Xist impacts Xi chromatin accessibility, we performed ATAC-Seq in female mouse fibroblasts harboring an Xi on which Xist was conditionally deleted after XCI establishment (Xa^{WT} $Xi^{\Delta Xist}$)[13,20]. These cells are hybrid and display an Xa of *Mus castaneus* (cas) origin and an Xi of *Mus musculus* (mus) origin, which allows allele-specific analysis. To increase available allelic read depth, we pooled two highly reproducible biological replicates performed in the wild-type (WT) and Xa^{WT} $Xi^{\Delta Xist}$ cell lines (Supplementary Fig. 1a, Supplementary Data Set 2). In WT cells, ATAC-seq data demonstrated a clear bias in accessibility on the Xa, as shown by the depletion of mus reads relative to cas reads (Fig. 1a), consistent with a previously published profile[14].

In Xist-deleted cells, the number of ATAC-seq peaks was substantially increased on the Xi (Fig. 1b), indicating a restoration of chromatin accessibility after ablating Xist. By identifying peaks with significant differences in allelic read counts in WT versus mutant cells, we categorized regions into four accessibility classes (Fig. 1c,d, Supplementary Fig. 1b, Supplementary Data Set 3). First, the “Xi-only” regions (0.5%) comprised areas accessible only on the Xi in both WT and mutant cells (Fig. 1c,d, Table 1). Second, the “Monoallelic” class was accessible exclusively on the Xa in both cell lines and accounted for the majority (84.3%) of all X-linked regions. Third, “Bi-allelic” regions (6.4%) were those accessible on both alleles, in both cell lines, and positioned adjacent to promoters of escapee genes which are immune to XCI[21–26] (Fig. 1c,d, Table 1).

Finally, there was a fourth intriguing new class — “Xi-restored” (8.8% - 37 regions) — which became bi-allelically accessible when *Xist* was deleted (Fig. 1c,d, Supplementary Fig. 1b). In all 37 cases, the restored peaks corresponded to regions exclusively accessible on Xa in WT cells and were not randomly scattered *de novo* accessibility events. Principal component analysis (PCA) clearly distinguished between the three major accessibility classes using only two principle components, suggesting that a linear model can be trained to classify allelic read counts based on features that enabled derivation of the three major accessibility classes (Fig. 1e). Targeted allele-specific FAIRE-qPCR (Supplementary Fig. 1c) and ATAC-seq replicates performed on an independently derived Xa^{WT} $Xi^{\Delta Xist}$ cell line, as well as on a second WT fibroblast cell type, yielded similar results and confirmed the existence of an Xi-restored class (Supplementary Fig. 2a-f). Altogether, these data suggest that Xist is responsible for chromatin accessibility repression at specific Xi regions.

To assess Xist binding patterns on the Xi-restored regions, we employed allele-specific CHART-seq of WT cells[12] (Fig. 2). This analysis revealed a gradient of Xist binding on the Xi. Accessible Bi-allelic and Xi-only (*Firre [functional intergenic repeating RNA element]*) regions (Fig. 2a–c) showed the least Xist binding in WT cells — consistent with their chromatin being accessible and their corresponding genes being expressed. Monoallelic regions showed intermediate Xist coverage and the positive coverage was consistent with their being silent and inaccessible on the Xi (Fig. 2a–c). Most intriguingly, Xist preferentially targets Xi-restored regions (Fig. 2a–c). Thus, regions sensitive to Xist depletion were in general those that exhibited the greatest Xist binding levels in WT cells.

Taken together, CHART and ATAC data suggest that Xi chromatin is not homogeneously regulated and that Xi regions are differentially dependent on Xist for suppression of chromatin accessibility during XCI maintenance.

Because Xist depletion induces Xi chromatin re-accessibility, we carried out allele-specific RNA-seq to investigate gene re-activation. To identify genes sensitive to Xist depletion, we subclassified X-linked genes by employing a support vector machine (SVM) classifier model trained on allelic reads counts of the three major accessibility classes. The vast majority of RefSeq genes (90.7%) were classified as Monoallelic in expression, while the remaining 9.3% were classified as Bi-allelic in expression (Supplementary Fig. 2g, Supplementary Data Set 4). None of the RefSeq genes were classified as Xi-restored (i.e., reactivated) by the SVM model across two biological replicates. This demonstrated that Xi-restored accessibility peaks were not accompanied by genes reactivation. Interestingly, we observed a direct correlation between the distance of TSS to the closest ATAC-peak and the gene expression level (Supplementary Fig. 2h). Genes with accessible regions within 1 kb of their TSS manifested the highest expression levels. These findings suggest that the Xi-restored regions are not directly linked to gene expression alterations (Supplementary Fig. 2g) and as such are likely to correspond to distal regulatory elements rather than to gene promoters (Supplementary Fig. 2h).

Epigenetic attributes of Xi re-accessible regions

Next, we examined peak distributions of the accessibility classes over genomic features and observed that Xi-restored peaks were distinct from all other classified ATAC peaks (Fig. 3a,b); a large percentage of regions that became accessible after Xist loss therefore appeared to correspond to distal regulatory elements, rather than promoter elements, whereas the Monoallelic and Bi-allelic peaks tend to localize more frequently in the promoter region.

We then searched for known transcription factor motifs, as well as *de novo* motifs within ATAC peaks to identify potential defining features for each class. We observed that the Monoallelic class was enriched for the binding motif of transcription factor SP1, whereas the Bi-allelic class was enriched for the architectural factor CTCF (Fig. 3c, Supplementary Note 1a,b, Supplementary Data Set 5). These observations are consistent with earlier studies showing that SP1 binds preferentially to the Xa and cannot be detected over Xi regulatory elements[22] and that most Xi ATAC-seq peaks localized within CTCF-binding sites[14]. On the other hand, our analysis showed that Xi-restored regions were enriched for a distinct set of transcription factors, including AP-1, NFE2L2, and ZNF691 motifs (Fig. 3c, Supplementary Note1c, Supplementary Data Set 5). Of particular interest, these motifs were recently found enriched within distal regulatory regions bound by BRG1-containing SWI/SNF nucleosome remodeling complexes[27] — an association of potential relevance given that SWI/SNF complexes help regulate chromatin accessibility.

We wondered whether Xist ablation could also influence chromatin compaction around Xi-restored regions. Thus, we performed allele-specific compaction studies using micrococcal nuclease (MNase) digestion over time followed by quantitative PCR (MNase preferentially releases nucleosomes from decompacted chromatin[28]). Greater MNase digestion was observed only on the Xi allele over the Xi-restored regions of the mutant, as evidenced by

the significantly decreased signals across the MNase time course (Fig. 3d, Supplementary Fig. 3a). Thus, ablating Xist in the post-XCI state clearly impacts both chromatin accessibility and compaction in an Xi-specific manner.

Xist is known to recruit Polycomb repressive complex 2 (PRC2) to the Xi, marking the Xi with the repressive histone modification, H3K27me3[12,18,19]. We analyzed allele-specific ChIP-seq analysis of WT cells[12] and observed a high degree of concordance between Xist CHART and H3K27me3 ChIP signals over the classified accessible regions (Fig. 2a,b, Fig. 3e,f). Indeed, metagene analysis revealed that the Bi-allelic class was depleted of both Xist and H3K27me3; the Monoallelic class showed moderate Xist and H3K27me3 coverage consistent with a repressed and inaccessible state on the Xi; and the Xi-restored class showed highest levels of Xist and H3K27me3 coverage of all (Fig. 2a,b, Fig. 3e,f). Taken together, these data demonstrate that (i) Xist RNA and the PRC2 mark are highly concordant at the regional level, and (ii) Xi-restored regions are generally marked by high levels of Xist and H3K27me3 in WT cells.

We then examined consequences of ablating *Xist* by performing allele-specific ChIP-qPCR in Xa^{WT} $Xi^{\Delta Xist}$ cells. We observed a decrease in H3K27me3 levels on the Xi within Monoallelic regions, as represented by *Mecp2, Taf1, Rpgr,* and *Prdx4* (Fig. 3g, Supplementary Fig. 3b), supporting previously published studies[20,21,29]. However, upon Xist depletion, the decrease in H3K27me3 levels was more pronounced within Xi-restored regions (Fig. 3g), consistent with the idea that these regions are especially sensitive to perturbation. Interestingly, ChIP-qPCR of H2AK119ub, a mark set by Polycomb repressive complex 1 (PRC1) showed similar results (Fig. 3h, Supplementary Fig. 3c). Altogether, these observations indicate that (i) Xi-restored regions normally have high Xist coverage and (ii) Polycomb marks within this class are highly sensitive to the loss of Xist.

Xist interacts with BRG1-SWI/SNF complexes

Our analysis revealed that Xi-restored peaks showed a strong enrichment of motifs known to be occupied by the SWI/SNF nucleosome remodeler BRG1 (Fig. 3c)[27], which promotes chromatin accessibility[30,31]. In addition, BRG1 has been identified as interactor of Xist[13]. Therefore, we asked whether BRG1 plays a role in defining accessibility of the Xi-restored regions. ChIP-qPCR for bulk histone H3 revealed significant Xi-specific reduction in H3 levels over Xi-restored regions when comparing Xist deletion cells to their wild-type counterparts (Fig. 4a, Supplementary Fig. 3d). This finding supports the idea that chromatin re-accessibility at the nucleosomal level involves nucleosome remodeling, potentially by SWI/SNF complexes.

To test the idea that Xist RNA directly interacts with BRG1, we carried out UV-RIP assay with BRG1 antibodies in WT female dermal fibroblasts. qRT-PCR of BRG1 pulldown material showed significant interaction with Xist but not with the different negative controls tested (Fig. 4b). The interaction was significantly lower in the absence of UV crosslinking, suggesting a direct interaction.

Next, we asked which region of Xist interacts with BRG1 *in vivo*. Xist is a 17–19 kb long noncoding RNA harboring six repeat elements defined A to F that are known to interact with

specific protein partners in order to regulate XCI[32]. To identify the interacting domain(s), we utilized a formaldehyde crosslink RIP-qPCR assay[33] that includes a brief sonication step aimed to lightly fragment RNAs. While no significant enrichment was observed for two negative controls (Gapdh and Smad4), positive controls (Neat1 and Malat1)[34–36] pulled down BRG1 (Fig. 4c). By applying this technique to Xist, we observed higher enrichment of Xist Repeats A, C, E, and F relative to other Xist regions (Fig. 4c). These data suggest that BRG1 interacts with broad regions within the Xist transcript.

We tested this interaction *in vitro* by an RNA pulldown assay using purified recombinant FLAG-tagged BRG1 proteins (Fig. 4d). To examine whether BRG1 preferentially binds Xist within a complex pool of cellular RNAs, we purified total RNA from female dermal fibroblasts and quantified the interaction between BRG1 and Xist. Pulldown of Xist by FLAG-BRG1 was significantly enriched compared to pulldown using negative controls such as uncoated beads or FLAG-BAF60 — a SWI/SNF accessory subunit that was not identified as an Xist binder in previous proteomic screens[13,37,38] (Fig. 4e).

To pinpoint specific binding regions, we tested individual subfragments of Xist *in vitro*. In a preliminary test, we carried out RNA pulldown assays using total RNA from Xa^{WT} $Xi^{\Delta Xist}$ supplemented with *in vitro*-transcribed Xist exon 1 (Fig. 4f,g). Significant enrichment of Xist exon 1 was observed regardless of where the PCR amplicons were placed within exon 1 (Fig. 4g). We then repeated the pull down experiment by supplementing with Xist subfragments encompassing Repeats A, B, C, D, E, or F (Fig. 4f,h). Consistent with in vivo fRIP (Fig. 4c), we observed strong BRG1 interactions with Repeats A, F, C, and E separately, but to a significantly lesser extent with Repeats B or D (Fig. 4h). Taken together, our *in vitro* and *in vivo* results strongly argue that Xist RNA interacts with BRG1 in a direct and specific manner, preferentially mediated by Repeats A, C, E, and F.

Xist binding inhibits BRG1 activities *in vitro*

These findings highlight a paradox, as BRG1 ATPase interacts with Xist (Fig. 4b-h), but promotes open chromatin[30,31]. Recent studies have suggested that interaction between RNA and epigenetic complexes could be inhibitory to their catalytic activity[39–41]. Thus, to investigate whether Xist influences BRG1 activity, we performed two *in vitro* assays using purified recombinant BRG1-containing SWI/SNF complex with in vitro-transcribed RNA species, and an assembled nucleosome array. First, we tested BRG1 nucleosome remodeling activity in the presence of increasing concentrations of Xist fragments and two control RNAs, Evf2 and tRNA (Fig. 5a **and** Supplementary Fig. 4a). Interestingly, all tested RNA molecules had the capacity to inhibit BRG1's remodeling activity to some extent. However, the degree of inhibition varied considerably between RNA fragments. Indeed, RNA species that can interact directly with BRG1 exerted greatest functional inhibition of BRG1 remodeling activity, independently of RNA length (Fig. 5a, Supplementary Fig. 4a and 4c). In multiple biological replicates, Xist Repeats C, E, F and A imposed greatest functional interference, as quantified by the IC_{50} — the concentration of RNA at which 50% of BRG1 is inhibited. Repeats B and D — which bound BRG1 to a substantially lower extent (Fig. 4) — showed less inhibition. The negative control tRNAs showed least inhibition, consistent with poor binding to BRG1.

We also examined BRG1 ATPase activity, a function that is required for BRG1 remodeling activity. Similar to nucleosome remodeling, RNA generally inhibited ATP turnover. However, the degree of inhibition varied according to the RNA's ability to bind BRG1, with good binders exhibiting a lower IC_{50} and nonspecific binders (tRNA) exhibiting a high IC_{50} (Fig. 5b, Supplementary Fig. 4b and 4c). We conclude that specific regions of Xist RNA bind and inhibit BRG1 activities, resolving the paradox that a gene-activating complex (BRG1) interacts with a gene-repressing factor (Xist).

Xi re-accessibility is BRG1-dependent

Since Xist represses BRG1 activity, we predicted that ablating Xist would induce Xi chromatin re-accessibility in a BRG1-dependent manner. To assess this, we performed ATAC-seq upon BRG1 depletion in WT cells using siRNAs (Supplementary Fig. 5a–c). As expected, depleting BRG1 resulted in a genome-wide decrease in chromatin accessibility (Fig. 5c, Supplementary Data Set 6). For the X-chromosome, the decrease was accentuated at regions classified as Xi-restored relative to the two other classes (Fig. 5d, Supplementary Data Set 6). Allele-specific analysis showed that the change occurred on the Xa in WT cells, as these regions are inaccessible even in presence of BRG1 on the Xi (Supplementary Fig. 5d, Supplementary Data Set 6). Thus, on the active X (Xa), the regions classified as "Xi-restored" require BRG1 for full chromatin accessibility in WT cells.

We then examined changes in accessibility in Xist deletion cells by performing ATAC-seq after BRG1 depletion (Supplementary Fig. 5e,f, Supplementary Data Set 6). Again, Xi-restored regions showed an accentuated decrease (Supplementary Fig. 5g, Supplementary Data Set 6). By comparing both cells lines we observed that the effect on Xi-restored regions was greater and more significant in mutant than in WT cells, which was not the case for the two other classes, suggesting that in Xist deleted cells, the Xi allele is also impacted.

By performing allelic analyses, we observed that both Xa and Xi were impacted within the Xi-restored regions in Xist deleted cells upon BRG1 knock-down (Fig. 5f, Supplementary Fig. 5h, Supplementary Data Set 6), where the loss was substantially greater than the loss observed within Monoallelic and Bi-allelic regions. Allele-specific FAIRE-qPCR experiments corroborated the loss of chromatin accessibility on both alleles at Xi-restored regions in Xist deletion cells (Supplementary Fig. 5i). Taken together, these results demonstrate that the restoration of chromatin accessibility on the Xi after Xist ablation depends on BRG1.

Previous reports showed that Xist could also interact with other chromatin-remodeling enzymes, SNF2H and CHD4[13,33]. However, ATAC-seq analysis of WT cells in which SNF2H or CHD4 was knocked-down (Supplementary Fig. 6) showed no significant differences in chromatin accessibility for any of the three classes (Supplementary Fig. 6). Collectively, these data argue for the specificity of BRG1 and suggest BRG1 as the primary chromatin-remodeling enzyme that interacts with Xist and positively regulates chromatin accessibility on the X-chromosome.

Xist repulses BRG1 *in vivo*

A Xist-mediated repulsion model was previously established by analysis of chromosome architectural factors[13]. To determine whether Xist could repel BRG1, we carried out Xist RNA-FISH and BRG1 immunostaining in WT female fibroblasts. Relative to the surrounding nucleoplasm, we observed a substantial depletion of BRG1 within the Xi territory, marked by the Xist RNA "cloud" (Fig. 6a, Supplementary Fig. 7a). Next, we asked if ectopically expressed Xist RNA could force BRG1 exclusion on an autosome. In a male mouse embryonic fibroblast line carrying an inducible Xist transgene[42], overnight induction of Xist resulted in a substantial depletion of BRG1 signals within the ectopic Xist cloud (Fig. 6a). Thus, Xist actively repels BRG1 from chromatin in cis.

To obtain a higher resolution, we used nChIP-seq (Supplementary Fig. 7b) and confirmed that BRG1 binding was elevated at nucleosomes flanking ATAC-seq peaks (Fig. 6b, Supplementary Fig. 7c), consistent with BRG1 mediating the chromatin accessibility[30,43].

We then performed allelic BRG1 nChIP-seq analysis and pooled two highly reproducible biological replicates for both WT and *Xist*-deletion cells in order to increase available allelic read depth (Supplementary Fig. 7d, Supplementary Data Set 2). As expected, in WT cells, there was a significant enrichment of BRG1 reads on the Xa (Supplementary Fig. 7e), consistent with the Xa harboring active chromatin. On the other hand, the Xi is nearly devoid of BRG1 binding, supporting our microscopy observations (Fig. 6a).

Upon Xist deletion, there was an increase in BRG1 occupancy on the Xi overall (Supplementary Fig. 7f). Next, we classified BRG1 peaks on the X chromosome into three deposition classes, by using our SVM model trained on allelic read counts of three major accessibility classes (Fig. 6c, Supplementary Fig. 7g, Supplementary Data Set 7). The vast majority of the BRG1 peaks were classified as Monoallelic (78%), while 5% were Bi-allelic, and 17% were classified as Xi-restored (Fig. 6c, Supplementary Fig. 7g).

We asked whether restored BRG1 peaks corresponded to ATAC-based "Xi-restored" regions. While there was only a 49% overlap between ATAC-based versus BRG1-based "Monoallelic" regions and only a 37% overlap for "Bi-allelic" regions, 73% of accessible restored regions also display BRG1 re-occupancy (Fig. 6d-f, Supplementary Fig. 7h). This strongly argues that re-accessibility is functionally related to the return of BRG1 to the Xi. Allele-specific nChIP-qPCR confirmed the general findings (Supplementary Fig. 7i). Taken together, these data support the ideas that (i) BRG1 is responsible for rendering chromatin accessible over "Xi-restored" regions, and (ii) one of Xist's roles is to repel BRG1 from these Xi regions.

BRG1 potentiates Xi reactivation following drug treatment

Previous studies have demonstrated that, although Xi silencing is robust, partial Xi-reactivation can be achieved by ablating *Xist* and treatment with various drug inhibitors in combination[13,44–48]. To determine whether BRG1 affects Xi reactivation, we analyzed transcriptomic data[13] from WT fibroblasts treated with DNA methylation inhibitor (5'-azacytidine [aza]) and a Topoisomerase 2b inhibitor (etoposide [eto]), treated with a control shRNA (shCTL) versus those treated with shBRG1. Interestingly, the majority (77.3%) of Xi

re-activated genes was less re-activated in shBRG1-treated cells in comparison to shCTL-treated cells (Fig. 7a), suggesting that BRG1 stimulates Xi-reactivation upon drug treatment.

We then investigated if there is differential drugs sensitivity between the three accessibility classes. We analyzed the chromatin accessibility level upon aza+eto treatment in wild-type cells treated with siBRG1 compared to siCTL treated cells by performing ATAC-qPCR assays. Our molecular assays revealed that Xi-restored regions were significantly more susceptible to gain accessibility upon drug treatment compared to Monoallelic regions (Fig. 7b). Drug-dependent re-accessibility of these Xi-restored regions was substantially diminished in siBRG1 cells (Fig. 7b). These data demonstrate that BRG1 potentiates Xi reactivation following drug treatment.

Xist inhibits accessibility around escapee genes

We looked for patterns in the epigenomic landscape that might predispose Xi-restored regions to re-accessibility. Peak distributions along the Xi confirmed the close correlation between ATAC- and BRG1-restored peaks (Fig. 7c). The nonrandom pattern of re-accessibility suggests the possible existence of structural “hotspots”. Re-accessible regions were often found in close proximity to restored topologically associated domains (TADs) (Fig. 7c), which were shown to re-appear at select Xi locations when Xist is deleted[13,21]. Overall, 85% of Xi-restored regions occurred within restored TADs, which was substantially different from the ~30% observed for Monoallelic regions (Fig. 7d). Interestingly, >80% of restored BRG1 peaks were also significantly associated with restored TADs (Fig. 7d). This positive association with restored TADs was also observed for the Bi-allelic class, as defined by both ATAC and BRG1 peaks, indicating that restoration of BRG1 binding and accessibility tends to occur in proximity to active chromatin.

We noticed that restoration of BRG1 binding upon Xist ablation tends to originate from pre-existing BRG1 peaks on the Xi (Fig. 7e, Supplementary Fig. 8). Notably, 85% of all BRG1 Bi-allelic peaks displayed nearby BRG1 re-occupation (Supplementary Fig. 8). This observation further supported a non-random pattern of restoration and suggested that new BRG1 complexes are guided by pre-bound BRG1. Strikingly, the overall distance of Xi-restored BRG1 peaks to the nearest Bi-allelic peaks was substantially shorter than for peaks residing within the Monoallelic class (Fig. 7f). The same was true when comparing ATAC peaks (Fig. 7f). These pre-bound BRG1 peaks were generally located around genes that escape XCI (Fig. 1, Fig. 6). Thus, in the unperturbed state, Xist safeguards inaccessible chromatin from nearby open regions that harbor escapees. Loss of Xist leads to a susceptibility of nearby chromatin to BRG1 encroachment and re-accessibility.

We furthermore observed that SMC1a, an architectural factor that was shown to re-appear within restored TADs after Xist depletion[13,21], was restored along the Xi in a pattern resembling Xi-restored ATAC and BRG1 peaks (Fig. 7c). By analyzing SMC1a ChIP-seq data performed in both cell lines[13], we found that 73% of Xi-restored ATAC regions displayed a restored SMC1a peak (Fig. 7g, Supplementary Fig. 9a,b). Thus, SMC1a tends to re-appear in the Xi-restored locations when Xist is eliminated. At a genome-wide scale, we found that a quarter of all SMC1a peaks displayed ATAC peaks within ±1.5 kb (Supplementary Fig. 9c). The vast majority of SMC1a peaks overlapped tightly with

accessible peaks and their loss following BRG1 depletion occurred to a greater degree than seen at more distal SMC1a sites (located ~400 bp away) (Supplementary Fig. 9c). These findings indicate that BRG1 modulates accessibility at SMC1a binding sites on a genome-wide basis.

Finally, because chromatin of similar properties is thought to self-associate[5,49–51], we analyzed allele-specific Hi-C performed in WT and Xist deletion cells[13] and, intriguingly, found de novo hotspots of interaction between Xi-restored regions (Supplementary Fig. 10). This indicates the formation of “superloops” between distant Xi-restored regions. These superloops were specifically observed on the Xi of the Xist depleted cells, and not in WT cells (Supplementary Fig. 10), nor on the Xa of either cell line (data not shown). Taken together, these data provide strong support for (i) large-scale 3D re-organization of the Xi when Xist RNA is ablated, and (ii) the notion that re-accessible chromatin has a tendency to self-associate.

DISCUSSION

Here we have shown that BRG1 SWI/SNF complexes play an important role in defining chromatin accessibility for specific regions of the X-chromosome. Xist directly binds BRG1 and functionally antagonizes recruitment of associated SWI/SNF complexes to the Xi. The SWI/SNF core subunits, BAF155, BAF170 and BAF47, are critical for enabling the remodeling activity of the complex[27,52], and all four core subunits interact with Xist RNA[13]. The functional antagonism between Xist and BRG1 is based on two properties: In vitro, physical interaction between Xist and BRG1 represses BRG1’s remodeling and ATPase activities. In vivo, Xist evicts BRG1-containing SWI/SNF complex from the Xi (Fig. 8a). Although these properties are distinct, interactions inside cells are likely to be very dynamic. In one possible model, Xist first binds BRG1, blocks its ATPase/remodeling activity, and then evicts BRG1 from the Xi chromatin in a step-wise fashion, but future research is required to fully elucidate the precise order of events. In the absence of Xist, BRG1 returns to particular regions of the Xi (the “Xi-restored regions”), restoring chromatin accessibility and binding of cohesins (Fig. 8a). In line with previous studies[21,53,54], restoration of BRG1 binding on the Xi is however insufficient for Xi-reactivation during XCI maintenance, suggesting that other chromatin modification pathways must be perturbed in parallel. Indeed, our data show that BRG1 potentiates Xi-reactivation when DNA methylation and Topoisomerase 2b are inhibited (Fig. 7a,b). Our findings thereby provide further insight into the mechanism of Xist action: Conceptually, this long noncoding RNA repels positive chromatin factors in addition to recruiting inhibitory factors. Thus, even as Xist recruits Polycomb repressive complexes and other epigenetic complexes[13,19,37,38], the RNA actively repels a growing list of complexes, including SWI/SNF (Fig. 4, 6) and cohesins[13].

Another intriguing finding is that, upon Xist ablation, BRG1 binding tends to be restored around pre-existing BRG1 binding regions, corresponding to escapees (Fig. 7e, Supplementary Fig. 8). This tendency may have a basis in the Xi CT organization. The Xi is partitioned into INC and collapsed ANC, where Xist is enriched[1,2] — the WT ANC is very limited and restricted to domains harboring escapees[1,55] (Fig. 8b). We speculate that, upon Xist removal, the ANC is extended to neighboring regions, concomitant with the restoration

of BRG1 occupancy and accessibility (Fig. 8). Thus, we propose that the proximity of Xi-restored regions to the ANC facilitates their restoration.

Our study also has implications for Xi 3D organization. Given that chromatin remodeling complexes can regulate binding of cohesin[56,57], and owing to the ability of BRG1 to govern accessibility at SMC1a binding sites (Fig. 7, and Supplementary Fig. 9), we suggest that BRG1 is required for cohesin restoration. We do not currently know the precise order of return, but our data indicate that co-restoration of BRG1, accessibility, cohesins, and TADs results in formation of *de novo* Xi superloops. Because the action of BRG1-containing SWI/SNF complexes is ATP-dependent, we predict that restoration of accessibility, TADs, and cohesins, as well as formation of superloops, would require ATP hydrolysis. Formation of superloops is in line with the idea of self-association of chromatin with the same properties[5,49–51,58]. It is intriguing, however, that escapee regions on the unperturbed Xi do not form similar superloops (at least not detectably in our female dermal fibroblasts Hi-C experiments). One possibility is that escapee regions in WT cells are encompassed in cramped ANC regions that limited their interaction and movement in the Xi CT. The extension of these ANC regions induced by Xist depletion allows them to be efficiently re-organized. We suggest that Xist actively safeguards against formation of accessible 3D structures, including de novo superloops and conventional TADs.

Finally, our study brings to light the differential dependence of the X-chromosome to BRG1 and further underscores the emerging concept of regional epigenetic differences along the 166-Mb chromosome[13–15]. BRG1 is generally associated with enhancement of chromatin accessibility and in fact binds throughout the Xa-chromosome at actively transcribed regions (Fig. 5, 6). However, only 10–20% of the X-chromosome is affected by perturbations to the Xist-BRG1 interaction, whether by deleting *Xist* or by knocking down BRG1 (Fig. 1 and Fig. 5). This implies that other SWI/SNF or other remodeling complexes may cooperate and/or regulate accessibility of other regions of the X-chromosome. The fact that the Xi is not monolithic from an epigenetic perspective has pharmacological implications for X-linked diseases. As Xi-reactivating approaches gain feasibility for restoring expression of missing proteins in Rett, CDKL5 Syndromes, and other X-linked disorders[44–46,48], further understanding of how to selectively turn on genes or regions on the Xi would be of tremendous benefit. Our current study reveals that BRG1 potentiates Xi-reactivation upon drug treatment (Fig 7a,b) and thus suggests future approaches by which targeting BRG1-Xist interaction possibly in combination with DNA demethylation agents could enhance selectivity of Xi-reactivation.

ONLINE METHODS

Cell lines and siRNA transfection

Fibroblast lines Xa^{WT} $Xi^{\Delta Xist}$, ♀X+P and ♂X+P have been described elsewhere[13,20,42], and were negative for mycoplasma contamination. For depleting BRG1, SNF2H or CHD4, 30,000 cells were transfected with Dharmacon siRNAs (L-041135-00-0005, L-041484-01-0005, L-052142-00-0005, respectively) at a final concentration of 20 nM using a Lipofectamine RNAiMAX (Invitrogen) reverse transfection protocol. Control cells were transfected with control siRNAs (D-001810-10-05) under identical conditions. Knockdown

of target genes was confirmed by qRT-PCR and western blotting. All experiments were performed 48 hours post transfection.

Assay for Transposase-Accessible Chromatin with high-throughput sequencing

50,000 cells were washed briefly in cold PBS and permeabilized with cold lysis buffer (10 mM Tris-HCl, pH 7.4, 10 mM NaCl, 3 mM $MgCl_2$, 0.1% IGEPAL CA-630) containing proteinase inhibitor cocktail (Roche). Nuclei were resuspended in 1X TD Buffer (Illumina FC-121–1030), and 2.5μL of Tn5 Transposase (Illumina FC-121–1030) were added. Transposition reaction was performed at 37°C for 30 min, and DNA was purified using a Qiagen MinElute Kit. DNA libraries were amplified for a total of 8 cycles. Libraries were assessed for quality control on the BioAnalyzer 2100 (Aglient) to ensure nucleosomal phasing and complexity. Sequencing was performed on the HiSeq 2500 (Illumina), using 50 bp paired-end reads.

For ATAC-qPCR, fibroblast cells were treated daily with dimethyl sulfoxide or with 0.3 mM azacytidine + 0.3 mM Etoposide for 3 days. Chromatin accessibility values were normalized to those obtained on the Gapdh and Actn1 (positive controls) loci. Xi-restored regions serially numbered 1 to 4, correspond to genomic loci: chrX:75,835,000, chrX:73,476,670, chrX:94,048,210, and chrX:96,077,970, respectively. All sequences of primers used are designated in Supplementary Data Set 8.

ATAC-seq analysis

ATAC-seq libraries were subjected to high-throughput sequencing using an Illumina HiSeq 2500 apparatus according to manufacturer instructions. On average, approximately 40 million paired-end 50 bp reads were generated per every ATAC-seq sample (Supplementary Data Set 2). Adaptor sequences were trimmed with *Trim Galore! V0.4.1* (www.bioinformatics.babraham.ac.uk/projects/trim_galore/) (stringency 12 and allowed error rate 0.2). Identical genomic sequences (PCR duplicates) were removed by custom program prior to alignment. To account for the M. mus (mus) / M. castaneus (cas) hybrid character of mouse dermal fibroblast lines that were employed in a ChIP-seq studies, reads were first aligned to custom mus/129 and cas genomes, and then mapped back to the reference mm10 genome[59]. All alignments were performed by utilizing *bowtie2* (v2.2.7) in paired-end mode[60]. Post-processing of alignments was performed with custom scripts using *SAMtools*[61], and *BEDtools* (v2.25.0)[62]. These included accounting, alignment file-type conversion, extracting and reads sorting (*SAMtools*), and obtaining wig coverage files (*SAMtools depth*). Detailed description of all ATAC-seq analysis is provided in the Supplementary Note 2.

MNase kinetic assay

Cells were washed in PBS and nuclei were isolated with cold lysis buffer (10 mM Tris-HCl, pH 8, 10 mM $MgCl_2$, 0.25 M Sucrose, 1% Triton, 5 mM β-mercaptoethanol) containing proteinase inhibitor cocktail (Roche). Nuclei were washed three times and incubated in MN buffer (Tris-HCl pH 7.5 20 mM, NaCl 70 mM, KCl 20 mM, $MgCl_2$ 5 mM, $CaCl_2$ 3 mM). 100U of MNase (Worthington Biochemical Corporation) were added to initiate the kinetics. Adding EGTA and EDTA to a final concentration of 2 mM stopped the reaction. DNA was

purified and sensitivity to MNase was analyzed by qPCR. Undigested DNA was considered as Input and data were normalized to it. All sequences of primers used are designated in Supplementary Data Set 8.

Native Chromatin Immunoprecipitation assay

Approximately 50×10^6 cells were washed in PBS, scraped in lysis buffer (10 mM Tris-HCl pH7.5, 30 mM NaCl, 0.1% NP40, 3 mM $MgCl_2$ and proteinase inhibitor cocktail (Roche)) and incubated for 10 min on ice. After centrifugation, nuclei pellets were resuspended in benzonase buffer (50 mM Tris pH 7.5, 300mM NaCl, 0.5% NP40, 2.5mM $MgCl_2$ and proteinase inhibitor cocktail). Chromatin was digested by adding 125 units of benzonase (Sigma) for 30 min on ice and was spun at 16,000g at 4ºC. Benzonase digestion was stopped by diluting twice the supernatants in 50 mM Tris pH 7.5, 100 mM NaCl, 0.5% NP40, 15 mM EDTA containing proteinase inhibitor cocktail. After pre-clearing step using 100 µL Dynabeads protein G magnetic beads (Invitrogen), the chromatin was incubated with 4 µg of either anti-BRG1 (ab110641) or anti-IgG (Cell signaling, 2729S) antibodies pre-bound to 50 µl Dynabeads protein-G magnetic beads (Invitrogen) rotating for 4 hr at 4°C. An aliquot of untreated chromatin was processed in parallel and used as the total input DNA control. Beads were washed 3 times in 50 mM Tris pH 7.5, 150 mM NaCl, 0.5% NP40, 5mM EDTA, followed by 3 times in 50 mM Tris pH 7.5, 500 mM NaCl, 0.5% NP40, 5 mM EDTA. DNA was eluted twice by incubation in elution buffer (1% SDS, 0.1 M $NaHCO_3$) for 15 min. DNA was subjected to RNase and proteinase K digestion and then purified. Pulldown efficiencies were calculated by qPCR by using input as reference. Error bars were calculated as standard deviation of three biological replicates. All sequences of primers used are designated in Supplementary Data Set 8. For sequencing, 10 ng of IP or input DNA was used for ChIP-seq library construction using an NEBNext® Ultra DNA Library Prep Kit for Illumina®. Libraries were assessed for quality control on the BioAnalyzer 2100 (Aglient). Sequencing was performed on the HiSeq 2500 (Illumina), using 50 bp paired-end reads.

ChIP-seq analysis

ChIP-seq libraries were subjected to high-throughput sequencing using an Illumina HiSeq 2500 apparatus according to manufacturer instructions. On average, approximately 45 million paired-end 50 bp reads were generated per every ChIP-seq sample (Supplementary Data Set 2). Adaptor sequences were trimmed with Trim Galore! V0.4.1 (www.bioinformatics.babraham.ac.uk/projects/trim_galore/) (stringency 12 and allowed error rate 0.2). Identical genomic sequences (PCR duplicates) were removed by custom program prior to alignment. To account for the M. mus (mus) / M. castaneus (cas) hybrid character of mouse dermal fibroblast lines that were employed in a ChIP-seq studies, reads were first aligned to custom mus/129 and cas genomes, and then mapped back to the reference mm10 genome[59]. All alignments were performed by utilizing *novoalign* (v3.00.02) in paired-end mode (Novocraft Technology, Selangor, Malaysia). Post-processing of alignments was performed with custom scripts using *SAMtools*[61], and *BEDtools* (v2.25.0)[62]. These included accounting, alignment file-type conversion, extracting and reads sorting (*SAMtools*), and obtaining wig coverage files (*SAMtools depth*). Detailed description of all nChIP-seq analysis is provided in the Supplementary Note 2.

UV-RNA Immunoprecipitation assay

10×10^6 female wild-type female dermal fibroblasts per IP were cross-linked by exposure to UV light at 200 mJ energy (Stratagene 2400) in 10 mL ice-cold PBS and collected by scraping in PBS. Cell pellets were incubated on ice in lysis solution (1% NP40, 400U/ml RNase Inhibitor [Roche], protease inhibitor cocktail [Sigma], and 1 mM DTT (add fresh), in PBS, pH 7.9) for 10 min. Sodium deoxycholate to a final concentration of 0.5% were added and cells were incubated on rotation wheel for 15 min at 4°C, followed by DNase treatment (30 U of TURBO DNase I, 30 min at 37°C). Supernatants were collected after a spin, pre-cleared 1h at 4°C with Dynabeads protein-G magnetic beads (Invitrogen) and incubated in overnight rotation at 4°C with 2.5 μg of either mouse IgG (Millipore, 12–371) or BRG1 (G-7) (sc-17796 X) antibodies pre-bound to 40 μl Dynabeads protein-G magnetic beads. An aliquot of supernatants was processed in parallel and used as the total input RNA control. Beads were washed three times with PBS containing 1% NP40, 0.5% sodium deoxycholate, additional 150 mM NaCl (total 300 mM NaCl), 400U/ml RNase Inhibitor [Roche], protease inhibitor cocktail [Sigma], and 1 mM DTT (add fresh). Beads were resuspended in 100 μl TurboDNase I buffer with 10 U Turbo DNase, and 40 U RNase Inhibitor [Roche] for 30 min at 37°C. After washing three more times with the same wash buffer supplemented with 10 mM EDTA, beads were incubated with 10 mM Tris-HCl (pH 7), 100 mM NaCl, 1 mM EDTA, 100 μg of Proteinase K (Roche), and 0.5% SDS for 1 h at 55°C. RNA was isolated by TRIzol and reverse-transcribed with random primers (Promega) using a Superscript III reverse transcriptase (Invitrogen). Control reactions without reverse transcriptase (−RT) and without UV treatment (-UV) were performed in parallel. Pulldown efficiencies were calculated by qPCR using input as reference. All sequences of primers used are designated in Supplementary Data Set 8.

Formaldehyde-RNA Immunoprecipitation assay

10×10^6 female wild-type female dermal fibroblasts per IP were trypsinized for 3 min, trypsin was quenched by addition of 10 ml media containing FBS. After centrifugation, resuspended in media containing FBS and cross-linked for 10 min by addition of formaldehyde to a final concentration of 0.1% at room temperature. Cross-linking was then quenched by addition of 2.5M glycine (0.125M final concentration) and cells were incubated at room temperature. Crosslinked cells were spun at 300x g for 5 min at 4°C, flash froze and stored at −80 °C. Frozen cells were resuspended in RIPA lysis buffer (50 mM Tris (pH 8), 150 mM KCl, 0.1 % SDS, 1 % Triton-X, 5 mM EDTA, 0.5 % sodium deoxycholate, 0.5 mM DTT (add fresh), 400 U/ml RNase Inhibitor [Roche], and protease inhibitor cocktail [Sigma]) and incubated on a rotation wheel for 10 min at 4°C. Incubated cells were sonicated for 4 min in Covaris sonicator. After sonication, chromatin were spun at 16,000g at 4ºC 10 min. Supernatant was diluted by adding equal volume of fRIP binding/wash buffer (25 mM Tris (pH 7.5), 150 mM KCl, 0.5% NP-40, 5 mM EDTA, 0.5 mM DTT (add fresh), 400 U/ml RNase Inhibitor [Roche], and protease inhibitor cocktail [Sigma]), pre-cleared 1 hour at 4°C with Dynabeads protein-G magnetic beads (Invitrogen) and then incubated on rotation wheel for 2 hours at 4°C with 2.5 μg of either mouse IgG (Millipore, 12–371) or BRG1 (G-7) (sc-17796 X) antibodies. An aliquot of supernatants was processed in parallel and used as the total input RNA control. Then, 20 μL Dynabeads protein G magnetic beads (Invitrogen) per sample were added for two additional hours. Beads were washed twice with

1 mL of fRIP binding/wash buffer and were incubated with 10 mM Tris-HCl (pH 7), 100 mM NaCl, 1 mM EDTA, 100 μg of Proteinase K (Roche), and 0.5% SDS for 1 hour at 55°C and then another 1 hour at 65°C. RNA was isolated by TRIzol, DNAsed and reverse-transcribed with random primers (Promega) using a Superscript III reverse transcriptase (Invitrogen). Pulldown efficiencies were calculated by qPCR using input as reference. All sequences of primers used are designated in Supplementary Data Set 8.

In Vitro RNA Pulldown assay

40 pmol of BRG1-FLAG or BAF60-FLAG were immobilized with anti-FLAG M2 Magnetic Beads (Sigma) in PBS containing 0.05% bovine serum albumin, 0.1% NP-40, 1 mM ATP, 15 mM β-mercaptoethanol and proteinase inhibitor cocktail (Roche) for 2 hours. For in vitro RNA Pulldown performed with RNAs from WT cells, two micrograms of total RNAs from wild-type fibroblast cells were incubated with protein-bead complexes at room temperature for 2 hours in PBS containing 2 mM $MgCl_2$, 0.2 mM $ZnCl_2$, 15 mM β-mercaptoethanol, 100 U/ml RNase Inhibitor, 0.05% bovine serum albumin, 0.2% NP40, 1 mM ATP and proteinase inhibitor cocktail (Roche). For in vitro RNA Pulldown performed with RNAs from Xist-deleted cells with addition of Xist repeats RNAs, two micrograms of total RNAs from Xist-deleted fibroblast cells were incubated with 0.5 pmol of each in vitro transcribed Xist repeat RNA (using MEGAscript (Invitrogen)) and with protein-bead complexes at room temperature for 2 hours in PBS containing 2 mM $MgCl_2$, 0.2 mM $ZnCl_2$, 15 mM β-mercaptoethanol, 100 U/ml RNase Inhibitor, 0.05% bovine serum albumin, 0.2% NP40, 1 mM ATP and proteinase inhibitor cocktail (Roche). For in vitro RNA Pulldown performed with RNAs from Xist-deleted cells with addition of Xist exon-1 RNA, two micrograms of total RNAs from Xist-deleted fibroblast cells were incubated with 0.5 pmol of in vitro transcribed Xist exon-1 RNA (using MEGAscript (Invitrogen)) and with protein-bead complexes at room temperature for 2 hours in PBS containing 2 mM $MgCl_2$, 0.2 mM $ZnCl_2$, 15 mM β-mercaptoethanol, 100 U/ml RNase Inhibitor, 0.05% bovine serum albumin, 0.2% NP40, 1 mM ATP and proteinase inhibitor cocktail (Roche). RNAs were treated with TURBO DNase, TRIzol purified and renatured by heating and slow cooling. RNA-protein-bead complexes were washed four times with the same incubation buffer supplemented with additional 150 mM NaCl (total 300 mM NaCl). RNAs were eluted and extracted with TRIzol and then were reverse-transcribed with random primers (Promega) and Superscript III reverse transcriptase (Invitrogen). Control reactions without reverse transcriptase (−RT) were also prepared. RNA pulldown was then analyzed by qPCR. An aliquot of untreated RNA was processed in parallel and used as the total input RNA control. All sequences of primers used are designated in Supplementary Data Set 8.

Remodeling assays

Nucleosome arrays were assembled using Hela native histones on a Cy5 labeled template containing twelve 5S positioning sequences flanking a central dinucleosome (G5E4) site containing the recognition sequence for the HhaI endonuclease[63]. Baculovirus expression of the SWI/SNF complex was done essentially as described[52]. Reactions were carried out in 20-μL volume containing 8 mM HEPES (pH 7.9), 10 mM Tris (pH 7.7), 60 mM KCl, 120 ng/μl BSA, 4 mM $MgCl_2$ and 8% glycerol similar to prior reports[64]. Dilutions of the different RNAs were incubated with 5 nM SWI/SNF for 30 minutes at 30 °C prior to the

addition of 1 nM nucleosomes and 10 units of HhaI. Reactions were incubated for 1 hour at 30 °C before the addition of 10-μl of stop buffer (1.5 mg/ml Proteinase K, 70 mM EDTA, 10 mM Tris (pH 7.7), 1% SDS, 0.1% Orange-G). Reactions were incubated at 55 °C for 1 hour and then separated on a 1.2 % agarose gel in 1 X TAE. DNA was visualized on a Typhoon scanner and quantified using ImageQuant software. Apparent inhibition of remodeling was determined by the equation: ((fraction uncut with RNA and SWI/SNF) – (fraction uncut with SWI/SNF))/((fraction uncut without Brg1) – fraction uncut with Brg1)) and plotted using GraphPad Prism and fit to an equation for a sigmoidal curve.

ATPase assays

Mononucleosomes were assembled using recombinant histones on the Widom 601 positioning sequence with a 20 bp overhang[63]. Baculovirus expression of the SWI/SNF complex was done essentially as described[52]. Reactions were carried out in 20-μL volume containing 8 mM HEPES (pH 7.9), 10 mM Tris (pH 7.7), 60 mM KCl, 120 ng/μl BSA, 4 mM $MgCl_2$ and 8% glycerol similar to prior reports[64]. Dilutions of the different RNAs were incubated with 5 nM SWI/SNF for 30 minutes at 30 °C prior to the addition of 1 nM nucleosomes. Reactions were incubated for 1 hour at 30 °C before the addition of additional $MgCl_2$ to 10 mM. Following the manufactures instructions for ADP-Glo Max Assay (Promega) 25 μl of ADP-Glo Reagent was added to each reaction and incubated for 40 minutes at 25 °C. Then 50 uL of ADP-Glo Max Reagent was added and the reactions were allowed to incubate for a further hour at 25 °C. Luminescence was measured using a SpectraMax (Molecular Devices) plate reader. Apparent inhibition of ATPase activity was determined by the equation: 1-((luminescence with RNA and SWI/SNF) – (luminescence with SWI/SNF))/((luminescence without Brg1) – luminescence with Brg1)) and plotted using GraphPad Prism and fit to an equation for a sigmoidal curve.

Immunostaining and RNA-FISH assays

Cells were grown on coverslips (pre-incubated with 0.2% gelatin for 30 min), rinsed in PBS, and pre-extracted in 0.5% CSK-Triton supplemented with 10 mM ribonucleosidevanadyl complex (VRC) (New England Biolabs) on ice for 2 min. Cells were then washed once in CSK supplemented with 10 mM VRC, and incubated on ice for 2 min, followed by fixation by 4% paraformaldehyde in PBS at room temperature for 10 min. Cells were then washed twice with PBS and blocked in 1% bovine serum albumin in PBS containing RNase inhibitor (Roche) at room temperature for 20 min. Incubation was carried out at room temperature for 1 hr with primary antibodies raised against either BRG1 (ab110641) or H3K27me3 (Millipore, 07–449) in PBS containing 1% bovine serum albumin and RNase inhibitor (Roche). Cells were washed three times in PBS containing 0.02% Tween-20 (PBS-T). After incubating with secondary antibody at room temperature for 30 min, cells were washed three times in PBS-T. Cells were fixed again in 4% paraformaldehyde at room temperature for 10 min, washed twice in PBS and dehydrated in ethanol series. RNA FISH was performed using Cy3–labeled Xist probes for 6 hr at 37°C in a humid chamber. *Xist* was detected using nick translation of pSx9. Cells were washed three times in 2X SSC. The slides were then mounted with a drop of Vectashield with 4’,6-diamidino-2-phenylindole. Cells were observed under Nikon Eclipse 90i microscope equipped with 60X/1.4 N.A. objective lens, Orca ER charge-coupled device camera (Hamamatsu), and Volocity software

(Perkin Elmer). Image analysis was performed using Image J software. For the Xist induction experiments, Xist was induced overnight. Quantification of BRG1 intensity was represented as boxplots where horizontal line in each box interior represents median of BRG1 intensity values and the black cross indicates mean.

Statistics and reproducibility

All qPCR experiments (FAIRE-qPCR, ATAC-qPCR, MNase-qPCR, ChIP-qPCR, nChIP-qPCR, UV-RIP-qPCR, fRIP-qPCR, *in vitro* RNA Pulldown-qPCR, and RT-qPCR assays) were repeated at least three times as independent biological replicates and results are presented as mean ± s.d. For all qPCR results, the P values were calculated using two-tailed Student's t-test using GraphPad. All experiments presented as western blot images have been repeated twice with similar results. All sequencing experiments have been performed in two independent biological replicates, excepted for negative controls as ATAC-seq in siCHD4 and siSNF2H and nChIP-seq of IgG, where only one replicate has been sequenced. For all boxplot analysis from sequencing data, the P values were calculated using a one-sided non-parametric Wilcoxon test and the box boundaries represent 25th and 75th percentiles; centerline represents the median; whiskers indicate ±1.5 × interquartile range (IQR), and points are actual values of outliers. For all barplots analysis from sequencing data, the P-values were calculated using a one-sided two-proportion z-test.

Supplementary Material

Refer to Web version on PubMed Central for supplementary material.

ACKNOWLEDGEMENTS

T. Jégu is a European Molecular Biology Organization (EMBO) postdoctoral fellow (EMBO ALTF 1313–2015) and a young researcher Bettencourt Schueller Foundation awardee. R.E.K. is supported by NIH grant, R37-GM048405. This work was supported by funding to J.T.L. from the Rett Syndrome Research Trust, the LouLou Foundation, the National Institutes of Health (R01-DA36895), and the Howard Hughes Medical Institute.

REFERENCES

1. Smeets D et al. Three-dimensional super-resolution microscopy of the inactive X chromosome territory reveals a collapse of its active nuclear compartment harboring distinct Xist RNA foci. Epigenetics Chromatin 7, 8 (2014). [PubMed: 25057298]
2. Cremer T et al. The 4D nucleome: Evidence for a dynamic nuclear landscape based on co-aligned active and inactive nuclear compartments. FEBS Lett 589, 2931–43 (2015). [PubMed: 26028501]
3. Dixon JR et al. Topological domains in mammalian genomes identified by analysis of chromatin interactions. Nature 485, 376–80 (2012). [PubMed: 22495300]
4. Nora EP et al. Spatial partitioning of the regulatory landscape of the X-inactivation centre. Nature 485, 381–5 (2012). [PubMed: 22495304]
5. Rao SS et al. A 3D map of the human genome at kilobase resolution reveals principles of chromatin looping. Cell 159, 1665–80 (2014). [PubMed: 25497547]
6. Rao SSP et al. Cohesin Loss Eliminates All Loop Domains. Cell 171, 305–320 e24 (2017). [PubMed: 28985562]
7. Lee JT Gracefully ageing at 50, X-chromosome inactivation becomes a paradigm for RNA and chromatin control. Nat Rev Mol Cell Biol 12, 815–26 (2011). [PubMed: 22108600]
8. Disteche CM Dosage compensation of the sex chromosomes and autosomes. Semin Cell Dev Biol 56, 9–18 (2016). [PubMed: 27112542]

9. Monfort A & Wutz A Progress in understanding the molecular mechanism of Xist RNA function through genetics. Philos Trans R Soc Lond B Biol Sci 372(2017).
10. Robert Finestra T & Gribnau J X chromosome inactivation: silencing, topology and reactivation. Curr Opin Cell Biol 46, 54–61 (2017). [PubMed: 28236732]
11. Clemson CM, McNeil JA, Willard HF & Lawrence JB XIST RNA paints the inactive X chromosome at interphase: evidence for a novel RNA involved in nuclear/chromosome structure. J Cell Biol 132, 259–75 (1996). [PubMed: 8636206]
12. Simon MD et al. High-resolution Xist binding maps reveal two-step spreading during X-chromosome inactivation. Nature 504, 465–469 (2013). [PubMed: 24162848]
13. Minajigi A et al. Chromosomes. A comprehensive Xist interactome reveals cohesin repulsion and an RNA-directed chromosome conformation. Science 349(2015).
14. Giorgetti L et al. Structural organization of the inactive X chromosome in the mouse. Nature 535, 575–9 (2016). [PubMed: 27437574]
15. Darrow EM et al. Deletion of DXZ4 on the human inactive X chromosome alters higher-order genome architecture. Proc Natl Acad Sci U S A 113, E4504–12 (2016). [PubMed: 27432957]
16. Costanzi C & Pehrson JR Histone macroH2A1 is concentrated in the inactive X chromosome of female mammals. Nature 393, 599–601 (1998). [PubMed: 9634239]
17. Heard E et al. Methylation of histone H3 at Lys-9 is an early mark on the X chromosome during X inactivation. Cell 107, 727–38 (2001). [PubMed: 11747809]
18. Plath K et al. Role of histone H3 lysine 27 methylation in X inactivation. Science 300, 131–5 (2003). [PubMed: 12649488]
19. Zhao J, Sun BK, Erwin JA, Song JJ & Lee JT Polycomb proteins targeted by a short repeat RNA to the mouse X chromosome. Science 322, 750–6 (2008). [PubMed: 18974356]
20. Zhang LF, Huynh KD & Lee JT Perinucleolar targeting of the inactive X during S phase: evidence for a role in the maintenance of silencing. Cell 129, 693–706 (2007). [PubMed: 17512404]
21. Splinter E et al. The inactive X chromosome adopts a unique three-dimensional conformation that is dependent on Xist RNA. Genes Dev 25, 1371–83 (2011). [PubMed: 21690198]
22. Calabrese JM et al. Site-specific silencing of regulatory elements as a mechanism of X inactivation. Cell 151, 951–63 (2012). [PubMed: 23178118]
23. Wu H et al. Cellular resolution maps of X chromosome inactivation: implications for neural development, function, and disease. Neuron 81, 103–19 (2014). [PubMed: 24411735]
24. Finn EH, Smith CL, Rodriguez J, Sidow A & Baker JC Maternal bias and escape from X chromosome imprinting in the midgestation mouse placenta. Dev Biol 390, 80–92 (2014). [PubMed: 24594094]
25. Berletch JB et al. Escape from X inactivation varies in mouse tissues. PLoS Genet 11, e1005079 (2015). [PubMed: 25785854]
26. Marks H et al. Dynamics of gene silencing during X inactivation using allele-specific RNA-seq. Genome Biol 16, 149 (2015). [PubMed: 26235224]
27. Nakayama RT et al. SMARCB1 is required for widespread BAF complex-mediated activation of enhancers and bivalent promoters. Nat Genet 49, 1613–1623 (2017). [PubMed: 28945250]
28. Blank M et al. A tumor suppressor function of Smurf2 associated with controlling chromatin landscape and genome stability through RNF20. Nat Med 18, 227–34 (2012). [PubMed: 22231558]
29. Nozawa RS et al. Human inactive X chromosome is compacted through a PRC2-independent SMCHD1-HBiX1 pathway. Nat Struct Mol Biol 20, 566–73 (2013). [PubMed: 23542155]
30. Bao X et al. A novel ATAC-seq approach reveals lineage-specific reinforcement of the open chromatin landscape via cooperation between BAF and p63. Genome Biol 16, 284 (2015). [PubMed: 26683334]
31. Miller EL et al. TOP2 synergizes with BAF chromatin remodeling for both resolution and formation of facultative heterochromatin. Nat Struct Mol Biol 24, 344–352 (2017). [PubMed: 28250416]
32. Lu Z, Carter AC & Chang HY Mechanistic insights in X-chromosome inactivation. Philos Trans R Soc Lond B Biol Sci 372(2017).

33. D GH, Kelley DR, Tenen D, Bernstein B & Rinn JL Widespread RNA binding by chromatin-associated proteins. Genome Biol 17, 28 (2016). [PubMed: 26883116]
34. Kawaguchi T et al. SWI/SNF chromatin-remodeling complexes function in noncoding RNA-dependent assembly of nuclear bodies. Proc Natl Acad Sci U S A 112, 4304–9 (2015). [PubMed: 25831520]
35. Tang Y et al. Linking long non-coding RNAs and SWI/SNF complexes to chromatin remodeling in cancer. Mol Cancer 16, 42 (2017). [PubMed: 28212646]
36. Lino Cardenas CL et al. An HDAC9-MALAT1-BRG1 complex mediates smooth muscle dysfunction in thoracic aortic aneurysm. Nat Commun 9, 1009 (2018). [PubMed: 29520069]
37. McHugh CA et al. The Xist lncRNA interacts directly with SHARP to silence transcription through HDAC3. Nature 521, 232–6 (2015). [PubMed: 25915022]
38. Chu C et al. Systematic discovery of Xist RNA binding proteins. Cell 161, 404–16 (2015). [PubMed: 25843628]
39. Cifuentes-Rojas C, Hernandez A, Sarma K & Lee JT Regulatory interactions between RNA and Polycomb repressive complex 2. Molecular Cell ePub May 29, 2014(2014).
40. Kaneko S, Son J, Bonasio R, Shen SS & Reinberg D Nascent RNA interaction keeps PRC2 activity poised and in check. Genes Dev 28, 1983–8 (2014). [PubMed: 25170018]
41. Cajigas I et al. Evf2 lncRNA/BRG1/DLX1 interactions reveal RNA-dependent inhibition of chromatin remodeling. Development 142, 2641–52 (2015). [PubMed: 26138476]
42. Jeon Y & Lee JT YY1 tethers Xist RNA to the inactive X nucleation center. Cell 146, 119–33 (2011). [PubMed: 21729784]
43. de Dieuleveult M et al. Genome-wide nucleosome specificity and function of chromatin remodellers in ES cells. Nature 530, 113–6 (2016). [PubMed: 26814966]
44. Lessing D et al. A high-throughput small molecule screen identifies synergism between DNA methylation and Aurora kinase pathways for X reactivation. Proc Natl Acad Sci U S A 113, 14366–14371 (2016). [PubMed: 28182563]
45. Carrette LLG et al. A mixed modality approach towards Xi reactivation for Rett syndrome and other X-linked disorders. Proc Natl Acad Sci U S A 115, E668–E675 (2018). [PubMed: 29282321]
46. Bhatnagar S et al. Genetic and pharmacological reactivation of the mammalian inactive X chromosome. Proc Natl Acad Sci U S A 111, 12591–8 (2014). [PubMed: 25136103]
47. Minkovsky A et al. A high-throughput screen of inactive X chromosome reactivation identifies the enhancement of DNA demethylation by 5-aza-2′-dC upon inhibition of ribonucleotide reductase. Epigenetics & chromatin, 1–17 (2015). [PubMed: 25621012]
48. Sripathy S et al. Screen for reactivation of MeCP2 on the inactive X chromosome identifies the BMP/TGF-beta superfamily as a regulator of XIST expression. Proc Natl Acad Sci U S A 114, 1619–1624 (2017). [PubMed: 28143937]
49. Lieberman-Aiden E et al. Comprehensive mapping of long-range interactions reveals folding principles of the human genome. Science 326, 289–93 (2009). [PubMed: 19815776]
50. Bickmore WA & van Steensel B Genome architecture: domain organization of interphase chromosomes. Cell 152, 1270–84 (2013). [PubMed: 23498936]
51. Bonev B et al. Multiscale 3D Genome Rewiring during Mouse Neural Development. Cell 171, 557–572 e24 (2017). [PubMed: 29053968]
52. Phelan ML, Sif S, Narlikar GJ & Kingston RE Reconstitution of a core chromatin remodeling complex from SWI/SNF subunits. Mol Cell 3, 247–53 (1999). [PubMed: 10078207]
53. Wutz A & Jaenisch R A shift from reversible to irreversible X inactivation is triggered during ES cell differentiation. Mol Cell 5, 695–705 (2000). [PubMed: 10882105]
54. Csankovszki G, Panning B, Bates B, Pehrson JR & Jaenisch R Conditional deletion of Xist disrupts histone macroH2A localization but not maintenance of X inactivation. Nat Genet 22, 323–4 (1999). [PubMed: 10431231]
55. Jegu T, Aeby E & Lee JT The X chromosome in space. Nat Rev Genet 18, 377–389 (2017). [PubMed: 28479596]

56. Hakimi MA et al. A chromatin remodelling complex that loads cohesin onto human chromosomes. Nature 418, 994–8 (2002). [PubMed: 12198550]

57. Wiechens N et al. The Chromatin Remodelling Enzymes SNF2H and SNF2L Position Nucleosomes adjacent to CTCF and Other Transcription Factors. PLoS Genet 12, e1005940 (2016). [PubMed: 27019336]

58. Chadwick BP & Willard HF Multiple spatially distinct types of facultative heterochromatin on the human inactive X chromosome. Proc Natl Acad Sci U S A 101, 17450–5 (2004). [PubMed: 15574503]

59. Pinter SF et al. Spreading of X chromosome inactivation via a hierarchy of defined Polycomb stations. Genome Res 22, 1864–76 (2012). [PubMed: 22948768]

60. Langmead B & Salzberg SL Fast gapped-read alignment with Bowtie 2. Nat Methods 9, 357–9 (2012). [PubMed: 22388286]

61. Li H et al. The Sequence Alignment/Map format and SAMtools. Bioinformatics 25, 2078–9 (2009). [PubMed: 19505943]

62. Quinlan AR & Hall IM BEDTools: a flexible suite of utilities for comparing genomic features. Bioinformatics 26, 841–2 (2010). [PubMed: 20110278]

63. Luger K, Rechsteiner TJ & Richmond TJ Preparation of nucleosome core particle from recombinant histones. Methods Enzymol 304, 3–19 (1999). [PubMed: 10372352]

64. Narlikar GJ, Phelan ML & Kingston RE Generation and interconversion of multiple distinct nucleosomal states as a mechanism for catalyzing chromatin fluidity. Mol Cell 8, 1219–30 (2001). [PubMed: 11779498]

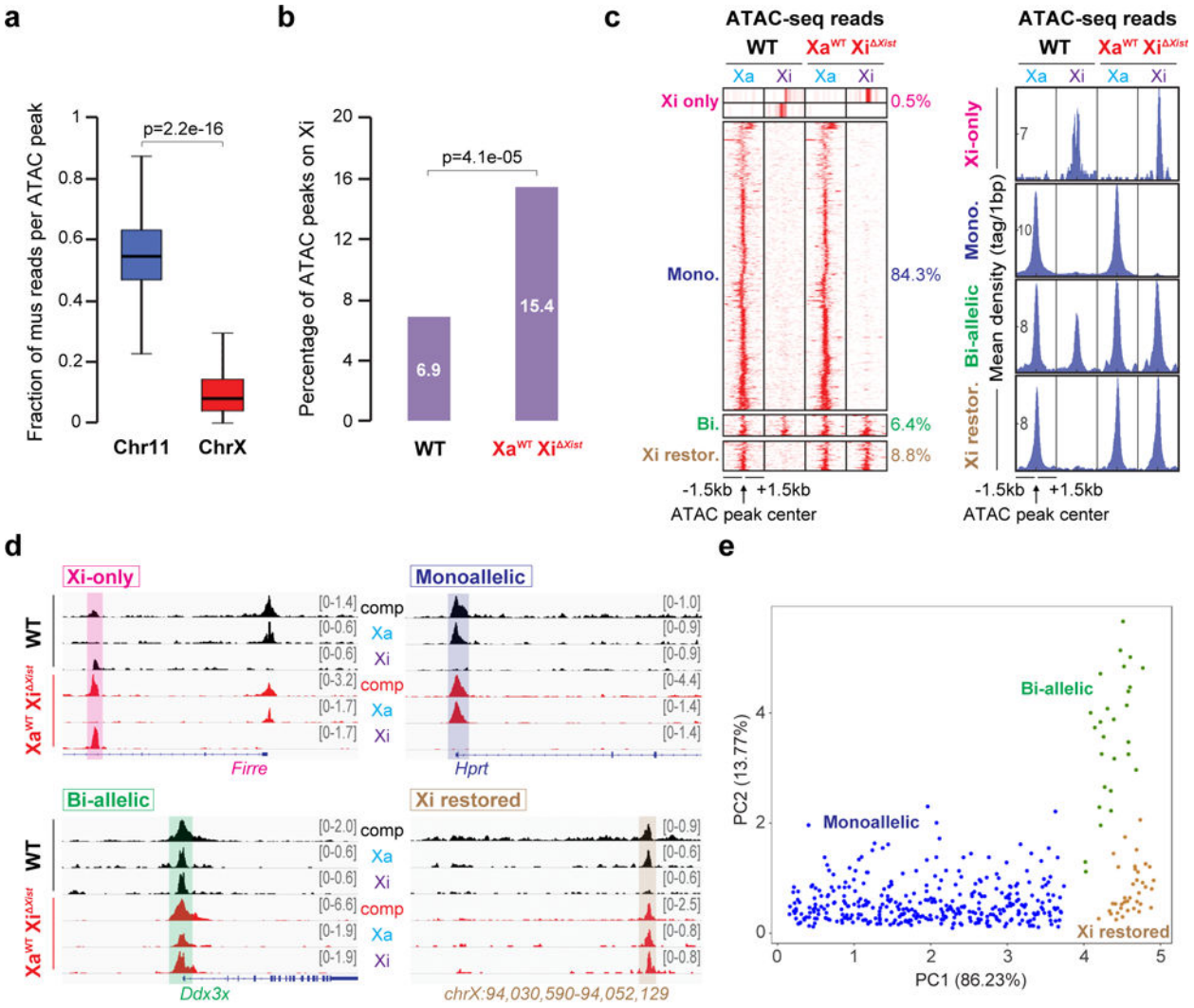

Figure 1. *Xist* deletion reveals four classes of accessible chromatin on the X-chromosome.

a. Boxplots showing distribution of differences in allelic skewing of ATAC-seq peaks in WT cells on chromosomes X (n=1,109) and 11 (n=2,295). P-value was determined using a one-sided non-parametric Wilcoxon test. Box boundaries represent 25th and 75th percentiles; centerline represents the median; whiskers indicate ±1.5 × interquartile range (IQR), and points are actual values of outliers. Xa, cas reads. Xi, mus reads. **b.** Comparison of percentages of ATAC peaks identified on Xi between Xa^{WT} $Xi^{\Delta Xist}$ and WT cells. P-value was determined using a one-sided two-proportion *z*-test. **c.** Left panel, allelic ATAC peak-centered heatmap of in Xa^{WT} $Xi^{\Delta Xist}$ and WT cell lines. ATAC peaks are divided into four classes by hierarchical clustering, and their relative percentage is designated on the right. Right panel, profiles presenting mean allele-specific ATAC signal of each class. **d.** Representative profiles for the four accessibility classes (highlighted). Similar results were obtained using another Xist deletion line. comp, all uniquely aligned reads. **e.** Principal component analysis (PCA) showing linear reduction of ATAC-Seq raw data (allelic reads counts) performed in mutant and WT cells.

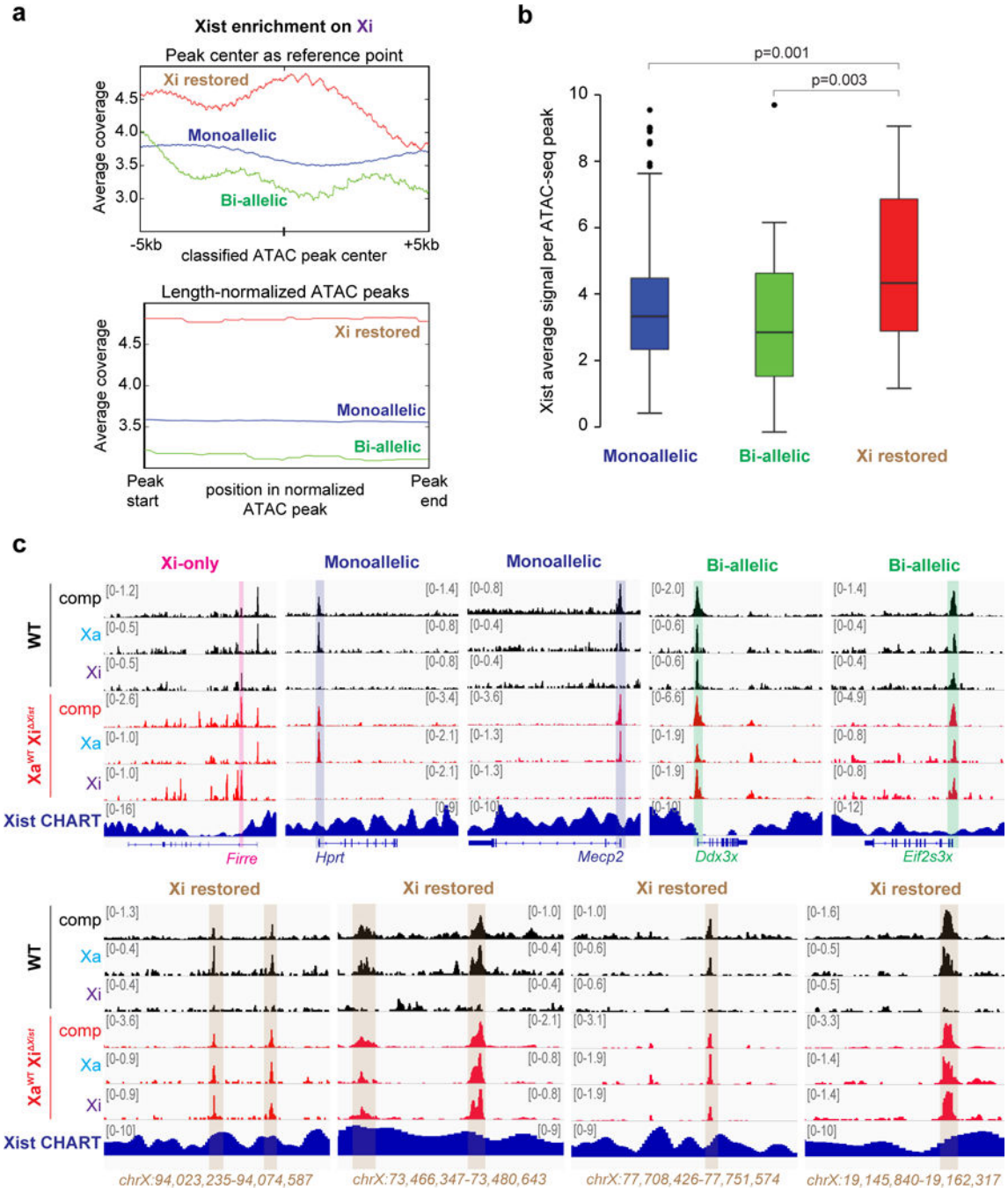

Figure 2. CHART-seq analysis demonstrates that Xi-restored regions normally have the greatest Xist RNA coverage and may be most dependent on Xist for silencing.

a. Average Xist CHART-seq signals on Xi in WT cells within the proximity of classified ATAC-seq peak centers (±5 kb). Unscaled reference-based profile (Top panel) and scaled regions profile (Bottom panel). **b.** Boxplots for each of the accessibility classes showing the distribution of Xist signals per ATAC-seq peak in WT cells; Monoallelic (n=356), Bi-allelic (n=27), and Xi-restored (n=37). Box boundaries represent 25th and 75th percentiles; centerline represents the median; whiskers indicate ±1.5 × interquartile range (IQR), and

points are actual values of outliers. P-values were determined using a one-sided non-parametric Wilcoxon test. **c.** Representative profiles of four ATAC accessibility classes and Xist CHART-seq signals on Xi in WT cells.

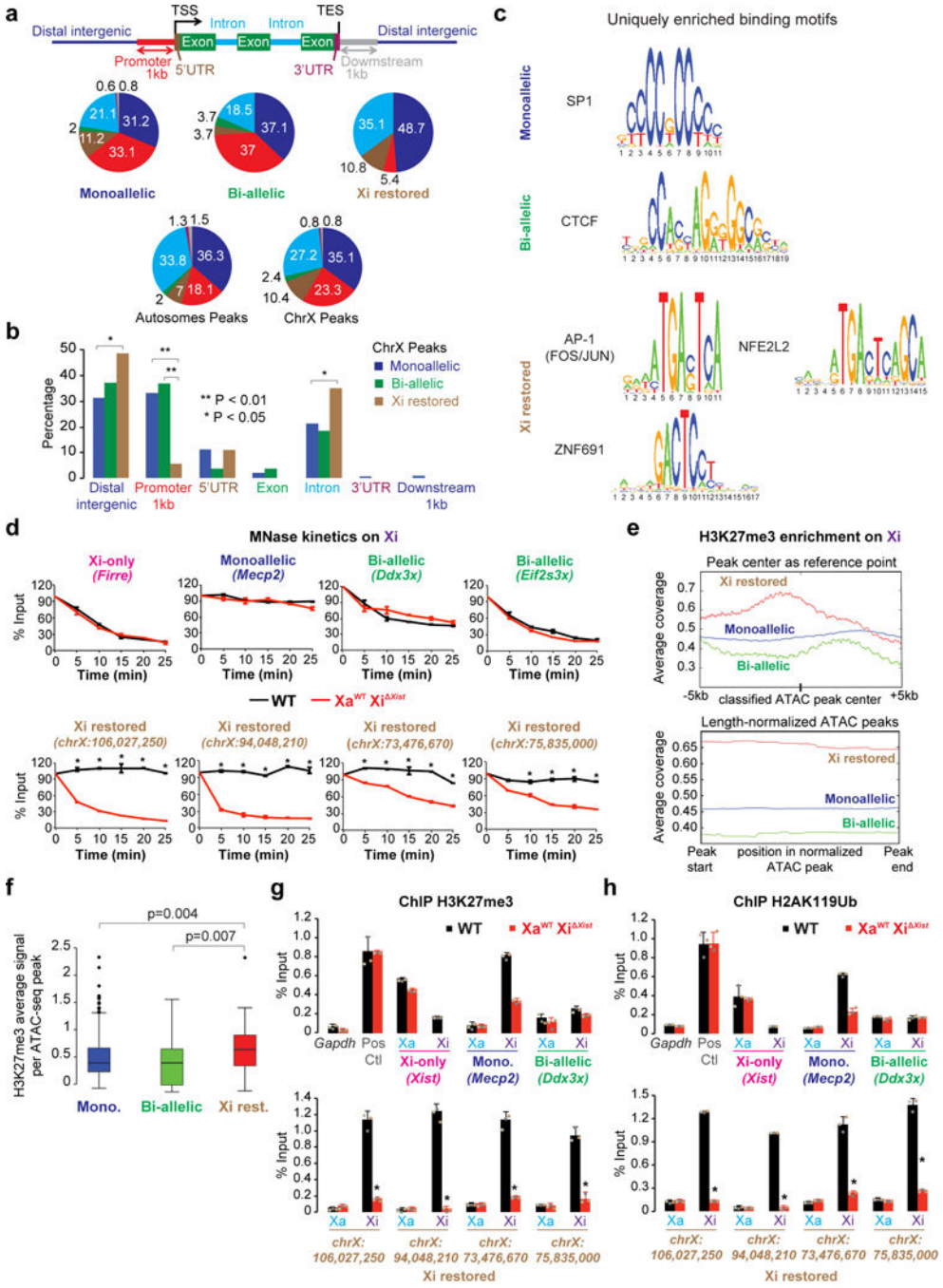

Figure 3. The epigenetic landscape of Xi-restored regions.

a. Percentage of ATAC-seq peaks from the three accessibility classes and two control groups (autosomal and X chromosomal ATAC-seq peaks) in indicated genomic regions. The upper panel illustrates a schematic of the analyzed genomic features. TSS, transcription start site. TES, transcription end site. **b.** Barplots of ATAC-seq peaks showing the percentage of each class annotated to indicated genomic features, Monoallelic (n=356), Bi-allelic (n=27), and Xi-restored (n=37). P-values were determined using a one-sided two-proportion *z*-test. **c.** Consensus motifs uniquely enriched in each of the three accessibility classes. **d.** Time-

course MNase sensitivity as measured by qPCR at representative Xi-restored genes and controls. Higher values express stronger tendency of chromatin to remain refractory to MNase digestion, thus indicative of increased chromatin compaction. Error bars represent mean ± s.d. P-value indicates significant difference relative to mutant cells (* $P < 0.005$; two-tailed Student's t-test, n=3 independent experiments). Min, minutes. **e.** Average H3K27me3 ChIP-seq signals on Xi in WT cells within the proximity of classified ATAC-seq peak center (±5 kb). Unscaled reference-based profile (Top) and scaled regions profile (Bottom). **f.** Boxplots for each accessibility class showing the distribution of H3K27me3 signals per ATAC-seq peak in WT cells, Monoallelic (n=356), Bi-allelic (n=27), and Xi-restored (n=37). Box boundaries represent 25th and 75th percentiles; centerline represents the median; whiskers indicate ±1.5 × interquartile range (IQR), and points are actual values of outliers.P-values were determined using a one-sided non-parametric Wilcoxon test. Enrichment levels of Polycomb repressive marks H3K27me3 (**g**) and H2AK119Ub (**h**) were measured by ChIP-qPCR in mutant and WT cells. Error bars represent mean ± s.d. P-value indicates significantly higher difference between the two cell lines relative to the difference observed on Xi chromosome within Monoallelic region (* $P < 0.01$; two-tailed Student's t-test, n=3 independent experiments). Pos Ctl, positive control. No signal was observed at *Xist* on the Xi allele in Xa^{WT} $Xi^{\Delta Xist}$ cells because the qPCR amplicon is localized in the deleted region.

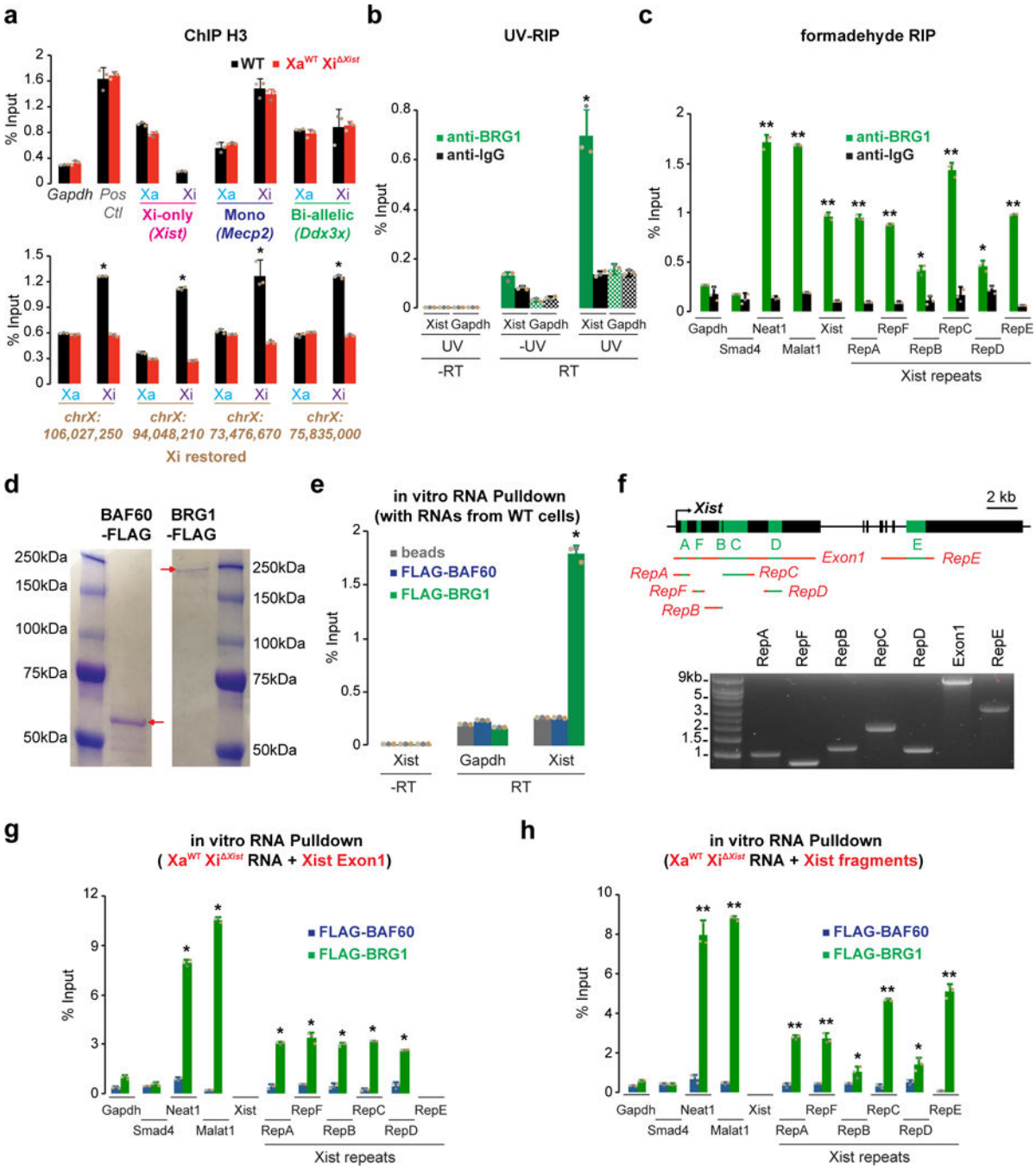

Figure 4. Xist directly interacts with BRG1.

a. H3 ChIP-qPCR performed in WT and mutant cells. Error bars represent mean ± s.d. P-value indicates significant differences compared with mutant cells (* P < 0.001; two-tailed Student's t-test, n=3 independent experiments). **b.** UV-crosslink RIP experiments performed in female dermal fibroblasts using BRG1 or IgG antibodies, followed by qRT-PCR for Xist and Gapdh. Error bars represent mean ± s.d. P-value indicates significant differences relative to IgG control (* P < 0.001; two-tailed Student's t-test, n=3 independent experiments). **c.** fRIP experiments performed in female dermal fibroblasts using BRG1 or IgG antibodies,

followed by qRT-PCR for 5 different RNAs and 6 different regions of Xist transcript (Rep A to F). Error bars represent mean ± s.d. P-values indicate significant differences relative to IgG control (* $P < 0.01$, ** $P < 0.001$; two-tailed Student's t-test, n=3 independent experiments). Significant differences between Rep A, F, C, and E relative to Rep B and D were also calculated ($P < 0.0005$; two-tailed Student's t-test). **d.** Coomassie stain of purified full-length FLAG-BAF60 (left) and purified full-length FLAG-BRG1 (right). **e.** *In vitro* RNA pulldown assay using purified FLAG-BAF60, FLAG-BRG1 or M2 beads and RNA isolated from WT female dermal fibroblasts. qRT-PCR was performed for Xist and Gapdh. Error bars represent mean ± s.d. P-value indicates significant difference relative to FLAG-BAF60 and beads controls (* $P < 0.0001$; two-tailed Student's t-test, n=3 independent experiments). **f.** Map of *Xist* locus (top panel). Black and green boxes correspond to exons and repeats, respectively; red lines represent *in vitro* transcribed RNAs. Agarose gel showing transcribed RNAs (bottom panel). **g.** RNA pulldown assay using purified FLAG-BAF60 or FLAG-BRG1 and Xa^{WT} $Xi^{\Delta Xist}$ female dermal fibroblasts RNAs with addition of Xist exon-1 RNA. qRT-PCR as in panel c. Error bars represent mean ± s.d. P-value indicates significant differences relative to FLAG-BAF60 control (* $P < 0.0002$; two-tailed Student's t-test, n=3 independent experiments). "Xist" and "Rep E" primers did not yield PCR product because the reverse primer resides within the 3rd or last exon of Xist, respectively, and not within exon-1. **h.** RNA pulldown assay using purified FLAG-BAF60 or FLAG-BRG1 and Xa^{WT} $Xi^{\Delta Xist}$ female dermal fibroblasts RNAs with addition of Xist repeats transcripts. qRT-PCR as in panel c. Error bars represent mean ± s.d. P-values indicate significant differences relative to FLAG-BAF60 control (* $P < 0.05$, ** $P < 0.005$; two-tailed Student's t-test, n=3 independent experiments). Significant differences between Rep A, F, C, and E relative to Rep B and D were also calculated ($P < 0.005$; two-tailed Student's t-test). Uncropped gel images for panels d and f are shown in Supplementary Data Set 1.

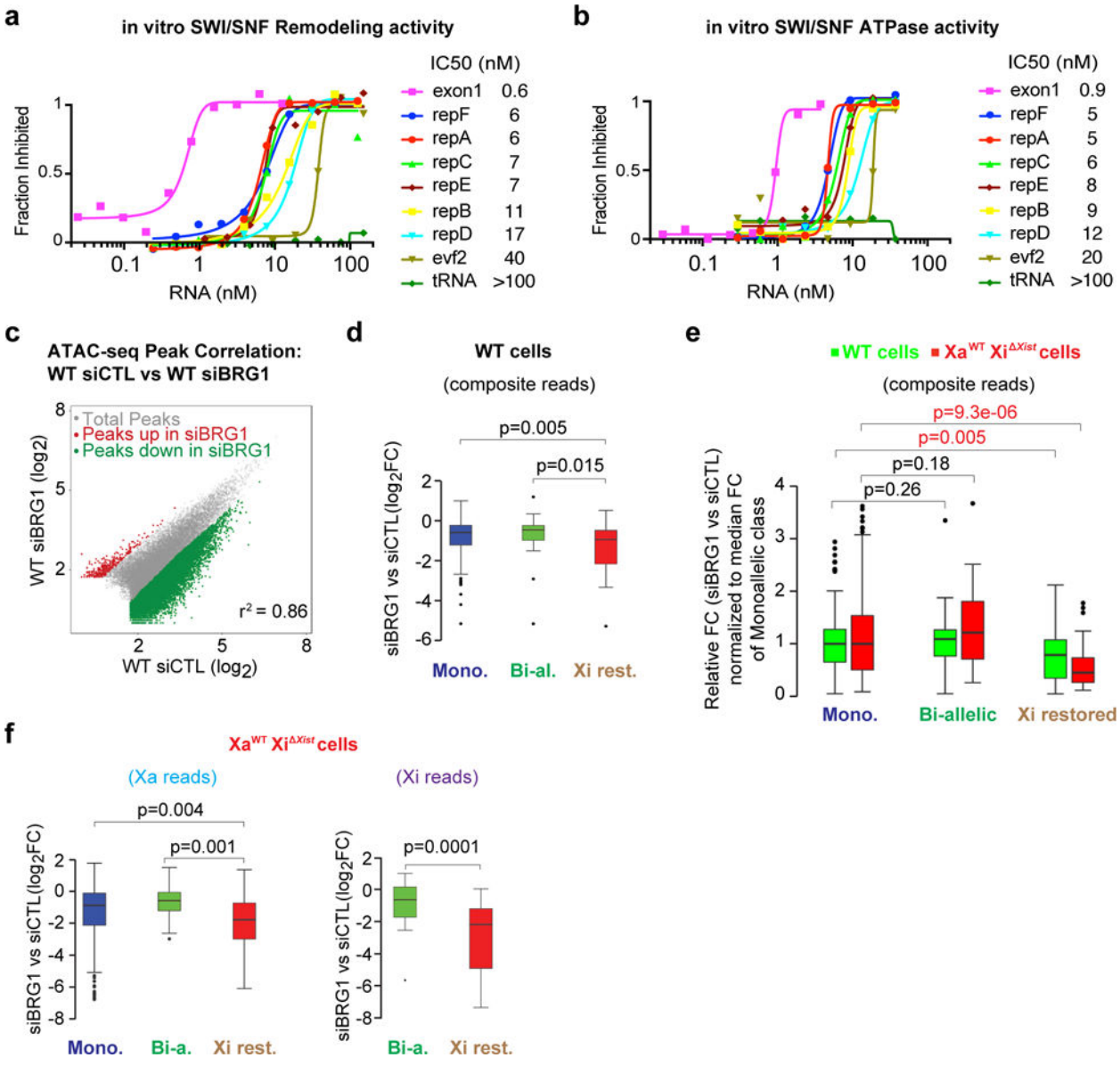

Figure 5. Xist RNA inhibits the catalytic activity of BRG1.

a,b. Quantification of SWI/SNF remodeling and ATPase activities in presence of the 9 indicated RNAs. IC50 represents concentration of RNAs generating 50% inhibition. Each graph is a representative of three independent experiments. **c.** Genome-wide scatter plots, using composite reads, showing chromatin accessibility changes between siBRG1 and siCTL treated WT cells. Peaks where chromatin accessibility was significantly increased (n=312) or decreased (n=10,200) as result of BRG1 depletion are highlighted in red or green, respectively (FDR<0.05). For each peak an average value was calculated from two independent experiments. r^2, Pearson correlation coefficient. **d.** Boxplots showing distribution of fold change accessibility values (log_2FC) between siBRG1 and siCTL treated WT cells. Fold change values between each condition were calculated based on all uniquely aligned reads (composite reads) of ATAC-seq peaks; Monoallelic (n=288), Bi-allelic (n=24), and Xi-restored (n=30). P-values were determined using a one-sided non-parametric

Wilcoxon test. **e.** Boxplots showing per class distribution of FC (siBRG1 versus siCTL) values normalized to their corresponding median FC value of the Monoallelic class (in the corresponding cell line), Monoallelic (n=288), Bi-allelic (n=24), and Xi-restored (n=30). P-values were determined using a one-sided non-parametric Wilcoxon test. **f.** Boxplots showing per class distribution of log_2FC (siBRG1 versus siCTL) accessibility values in Xist deletion cells. For each class, peaks signals were obtained from allelic reads of either Xa (left panel), Monoallelic (n=314), Bi-allelic (n=23), and Xi-restored (n=35), or Xi (right panel), Bi-allelic (n=20) and Xi-restored (n=32). P-values were determined using a one-sided non-parametric Wilcoxon test. Monoallelic class is not shown for Xi reads analysis because the Monoallelic class does not display Xi reads (Fig. 1c). For all Box blots, box boundaries represent 25th and 75th percentiles; centerline represents the median; whiskers indicate ±1.5 × interquartile range (IQR), and points are actual values of outliers.

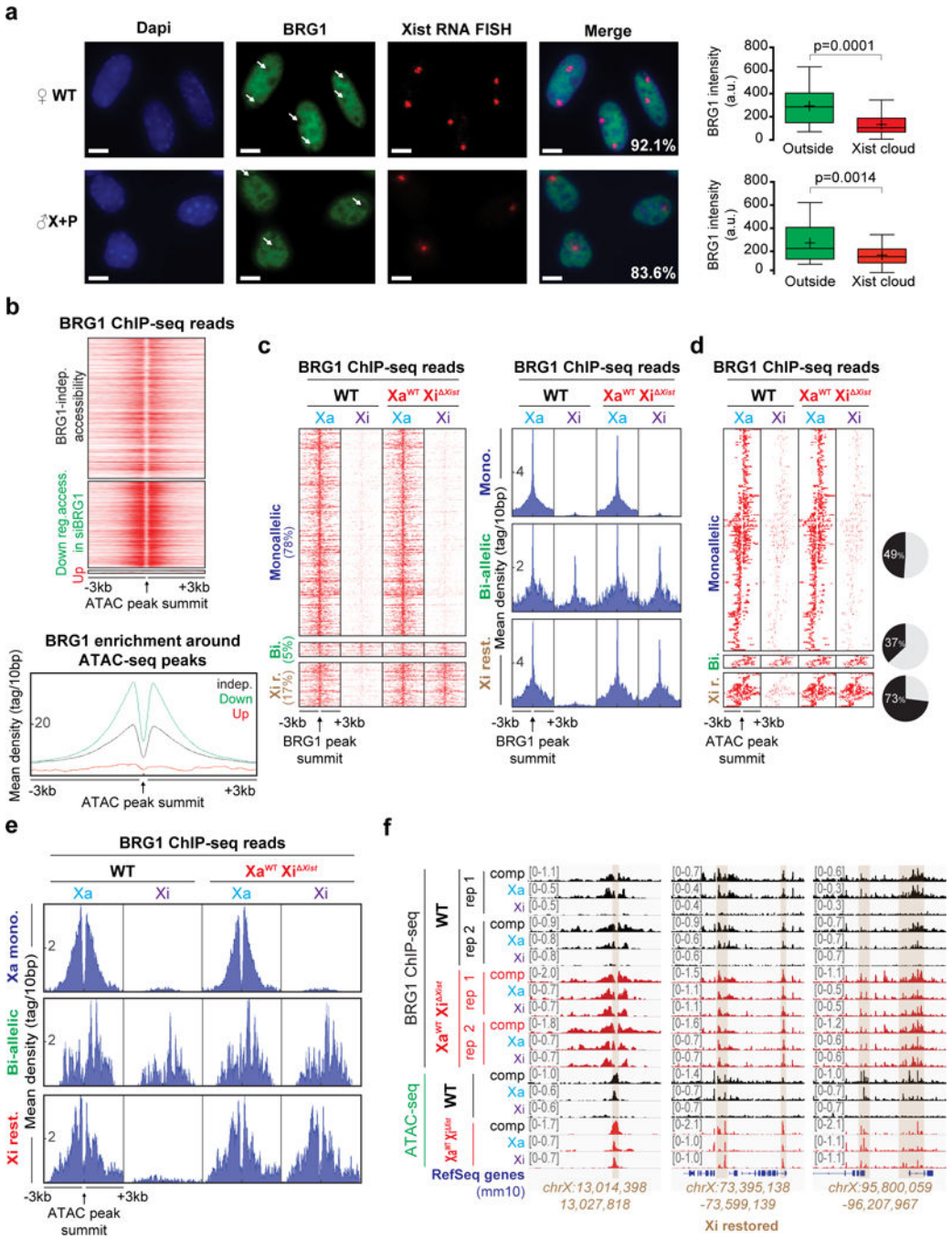

Figure 6. Xist evicts BRG1 from the Xi.

a. Immuno-RNA-FISH for BRG1 and Xist. Top row, female WT (♀ WT) fibroblasts, immortalized with SV40 large T-antigen and therefore tetraploid (4n). Bottom row, male MEF lines harboring a WT *Xist* transgene (♂X+P). Arrows indicate locations of Xist clouds. Percentages of cells displaying a decrease in BRG1 intensity inside of Xist cloud are shown. Scale bar, 5 μm. For each cell line, BRG1 intensities outside (green) and inside of the Xist cloud (red) were calculated using Image J software. Box boundaries represent 25th and 75th percentiles; centerline represents the median; whiskers indicate ±1.5 × interquartile range

(IQR), and points are actual values of outliers. P-values were determined using a two-tailed Student's t-test. n=105 cells. **b.** Top, ATAC-seq summit-centered heatmap of BRG1 ChIP-seq signal performed in WT cells. ATAC-seq peaks are clustered into BRG1-independent (indep.), down-regulated in siBRG1 (Down), and up-regulated in siBRG1 (Up) groups based on ATAC-seq analysis performed in siCTL and siBRG1 treated WT cells. Bottom, distribution profile presenting mean BRG1 ChIP-seq signal for each group. **c.** Left panel, BRG1 ChIP-seq summit-centered heatmap presenting allele-specific BRG1 ChIP-seq signal in mutant and WT cells. BRG1 ChIP-seq peaks are clustered into three BRG1 deposition classes (relative percentage is designated). Right panel, profiles presenting mean allele-specific BRG1 ChIP-seq signal around BRG1 peak summit for each of BRG1 deposition classes. **d.** ATAC-seq summit-centered heatmap of allele-specific BRG1 ChIP-seq signal in both cell lines per accessibility class. For each class, percentage of classified ATAC-seq peaks presenting the same corresponding BRG1 classified ChIP-seq peaks at the two flanking nucleosomes is designated (corresponding pie charts to the right). **e.** Profiles presenting mean allele-specific BRG1 ChIP-seq signal around ATAC-seq peak summit for each accessibility class. **f.** Representative examples of Xi-restored ATAC-seq peak regions displaying restoration of BRG1 binding.

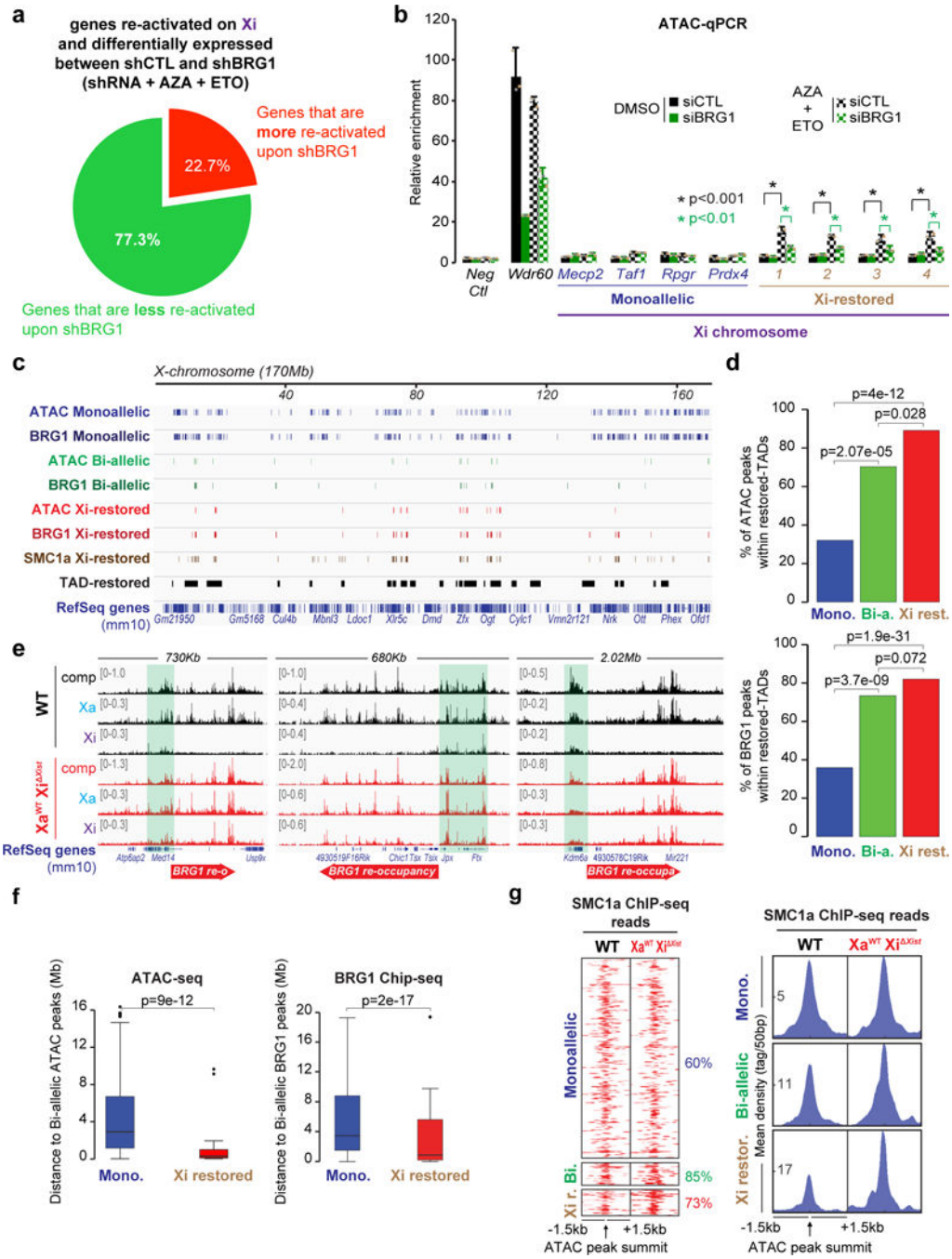

Figure 7. BRG1 re-occupancy extends from pre-existing BRG1 sites, and associate with restored cohesins and TADs.

a. Pie chart depicting percentage of genes that are more re-activated (FC >2) (red) or less re-activated upon stable BRG1 knock-down (FC <2) (green). **b.** Chromatin accessibility profiles measured by ATAC-qPCR in treated WT cells. Higher values indicate more accessible chromatin. Error bars represent mean ± s.d. P-values were determined using a two-tailed Student's t-test, n=3 independent experiments. Neg Ctl, negative control representing an inaccessible region. **c.** Chromosomal locations of three accessibility and

three BRG1 deposition classes, as well as restored TADs and cohesins regions across the Xi chromosome. **d.** Percentage of classified ATAC-seq (Top) and BRG1 (Bottom) peaks within restored-TADs, Monoallelic (n=356), Bi-allelic (n=27), and Xi-restored (n=37). P-values were determined using a one-sided two-proportion *z*-test. **e.** Representative examples of Xi-restored BRG1 binding patterns nearby pre-existing Bi-allelic BRG1-bound sites (highlighted). Red arrows indicate origin and direction of expansion of BRG1 re-occupancy on the Xi chromosome in Xist deleted cells. **f.** Boxplots showing distribution of distances in megabases (Mb) from Monoallelic (blue) or Xi-restored (red) peaks to nearest Bi-allelic peaks. Analyses were carried out for ATAC-seq (Top) and BRG1-seq (Bottom) classified peaks, Monoallelic (n=356), and Xi-restored (n=37). P-values were determined using a one-sided non-parametric Wilcoxon test. Box boundaries represent 25th and 75th percentiles; centerline represents the median; whiskers indicate ±1.5 × interquartile range (IQR), and points are actual values of outliers. **g.** Left panel, ATAC-seq peak summit-centered heatmap of SMC1a ChIP-seq signal (using composite reads) in both cell lines for each accessibility class. For each class, percentages of classified ATAC-seq peaks presenting significant SMC1a peaks within ±1.5 kb of the flanking region is designated (right). Right panel, profiles representing mean SMC1a ChIP-seq signal around ATAC-seq peak summits for each accessibility class.

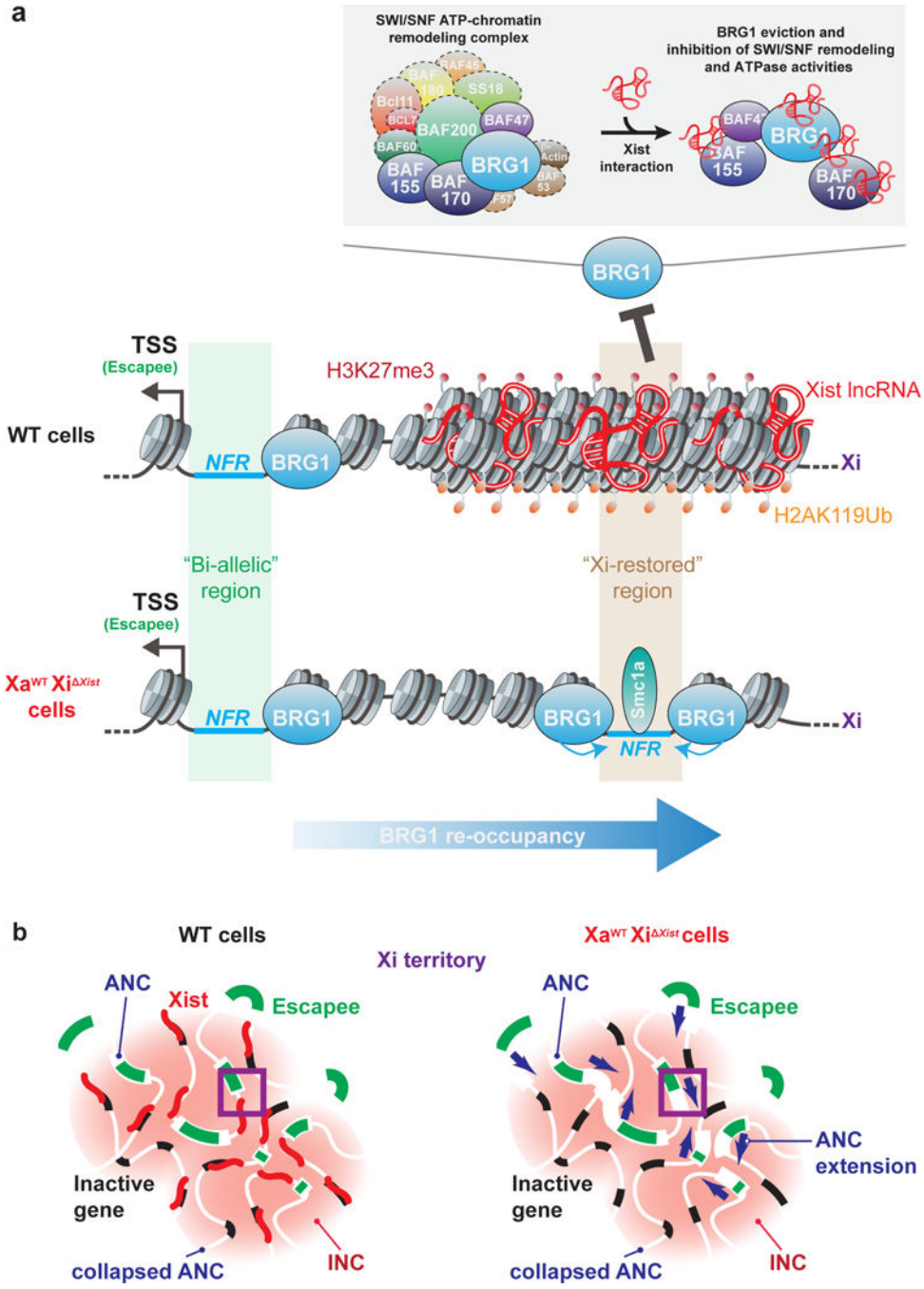

Figure 8. Model for Xist-BRG1 dynamics on the Xi.

a. On the unperturbed Xi (WT), Xist actively blocks remodeling and ATPase activities of BRG1 and repels BRG1 from the Xi (inset). BRG1 is normally only found within Bi-allelic escapee regions (and Xi-only regions) (highlighted green box). When *Xist* is deleted (Xa^{WT} $Xi^{\Delta Xist}$), BRG1 returns to Xi-restored regions (highlighted brown box), restoring chromatin accessibility (blue arrows) and binding of cohesins (SMC1a). BRG1 re-occupancy occurs nearby pre-existing BRG1 binding sites in Bi-allelic regions. TSS, Transcriptional Start Site. NFR, Nucleosome-Free Region. **b.** Within the Xi chromosome territory of WT cells, Xist

RNA is enriched in the collapsed active nuclear compartment (ANC) and escapee genes are localized in normal ANC (left panel). Upon Xist deletion, these ANCs expand to include Xi-restored regions (right panel). We propose that proximity to escapee ANCs predisposes Xi regions to restoration, potentially due to enrichment of activating chromatin factors. Purple squares denote region described in Fig 8a. INC, inactive nuclear compartment.

Table 1.

Genes displaying a classified accessibility peak at their proximal promoter site (±500 bp of TSS) on Xi chromosome in WT cells.

These genes correspond to previously reported escapee genes.

Xi-only	Bi-allelic
Firre	1810030O07Rik
Xist	Med14
	Ddv3x
	Kdm6a
	Utp14a
	Eif2s3x
	Jpx
	Ftx
	5530601H04Rik
	Tmem29
	Kdm5c
	Mid1